The Pennsylvania State University

The Graduate School

DETERMINING THE BOUNDS OF THE FREQUENCY STOP-BANDGAP IN ELASTODYNAMIC METASURFACES FOR S_0 LAMB WAVE EXCITATION

A Thesis in

Engineering Science and Mechanics

by

Jeremy D. Keirn

Submitted in Partial Fulfillment
of the Requirements
for the Degree of

Master of Science

May 2024

The thesis of Jeremy D. Keirn was reviewed and approved by the following:

Parisa Shokouhi
Professor of Engineering Science and Mechanics
Thesis Advisor

Clifford Lissenden
Professor of Engineering Science and Mechanics

Jacques Rivière
Assistant Professor of Engineering Science and Mechanics

Albert Segall
Professor of Engineering Science and Mechanics
Graduate Programs Officer

ABSTRACT

It has been shown that elastodynamic metasurfaces can be used to create a stop-bandgap for guided waves such as the fundamental symmetric Lamb wave mode (S_0 mode). These metasurfaces rely on the local resonances of surface-mounted resonators to hybridize with incident S_0 Lamb waves in a waveguide (i.e. a thin plate). This type of control of Lamb waves is achieved by tuning the resonator topology to apply an appropriate Auld boundary condition at its base when attached to a plate that is made from the same material. Recent studies for surface waves in bulk media have shown that there is a possible connection between the width of the bandgap and the resonances and antiresonances in the frequency response function (FRF) of the resonators under an appropriate base excitation. This study attempts to show that a similar connection exists for a locally resonant metasurface and the associated Lamb waves. Using a combination of simulations from COMSOL Multiphysics 6.2 and experiments on a 1 mm aluminum plate, it is shown that the width of the bandgap is determined by both the resonances and antiresonances of the resonators. With this understanding of the limits of the bandgap, a topology optimization process can be used to generate resonator geometries with increased distance between the resonances, which results in an increase in the width of the bandgap.

TABLE OF CONTENTS

LIST OF FIGURES

LIST OF TABLES

ACKNOWLEDGEMENTS

I would first like to thank my research advisor, Dr. Parisa Shokouhi, for all her guidance and support throughout this process. I would also like to thank the committee members, Dr. Clifford Lissenden and Dr. Jacques Rivière, for their time and feedback on my work. Special thanks to my colleagues in PennSUL, especially Lalith Sai Srinivas Pillarisetti and Daniel Giraldo Guzman, for their assistance and advice.

The author(s) gratefully acknowledge the support of the National Science Foundation under Grant No. 1934527. Any opinions, findings, and conclusions are those of the author(s) and do not necessarily reflect the views of the National Science Foundation.

Chapter 1 Introduction

The field of metamaterials has been rapidly expanding over the last few decades. A metamaterial is a type of engineered structure that can have a variety of unique properties due to a combination of its geometry and material composition. These structures can be designed to achieve various effects such as wave control. A specific type of metamaterial that applies to thin plates is called a metasurface. Recently, metasurfaces have been shown to be particularly adept for elastic vibration control [1 – 5]. The metasurfaces in these studies were created by attaching small, designed structures called resonators to thin plates made from the same material. These resonators are designed to use local resonances to enforce clamping boundary conditions on the plate at predetermined frequencies. The applied boundary conditions suppress wave propagation of the fundamental symmetric wave mode, also known as the S_0 Lamb wave mode, in the plate at those frequencies [3,4]. The range of frequencies where wave propagation is suppressed is known as a stop-bandgap, which can generally be referred to as just a bandgap.

Although these metasurfaces have been shown to be effective at suppressing the propagation of S_0 Lamb waves in thin plates at their designed frequencies, it is valuable to be able to achieve similar results over a larger range of frequencies. Previous studies used a variety of techniques to enhance the bandgap such as resonator grading [5 – 7]. However, these techniques still rely on designing individual resonators at different frequencies and combining them in an array to achieve larger bandgaps. There is a lack of rational methodologies for designing resonators that create larger bandgaps without the need for resonator grading. To create such a methodology, a parameter needs to be determined to be able to effectively predict the bounds of the bandgap based on the resonator geometry alone. A recent publication has shown that antiresonances and resonances of resonators that are used in a 3-dimensional metamaterial can be

used to predict the bandgap for surface waves in bulk media [8]. However, to the best of the author's knowledge, there has yet to be a similar analysis for 2-dimentional metasurface designs, which have different wave modes compared to bulk media. If a similar relationship exists, the frequency response function (FRF) could be used as a parameter to motivate an optimization process that aims to create resonators that have inherently larger bandgaps compared to more basic resonators.

This study aims to show that there is a connection between the FRF of an individual resonator design and the transmission spectrum of the corresponding metasurface creating using an array of resonators. Namely, it is expected that the antiresonances and resonances may be used to predict the bandgap in the transmission spectrum. To show this connection, a simple, prismatic resonator was considered for both numerical and experimental testing. Numerical models were created in COMSOL Multiphysics 6.2 to calculate the FRF, dispersion curves, and transmission spectra, and experimental results were used for verification of the transmission spectra. MATLAB was used to analyze and plot data from both sets of testing. Subsequently, a topology optimization was conducted based on the connection between the FRF and bandgap, and the resulting resonator geometry was tested numerically and compared to the prismatic resonator to show an increased bandgap width.

Chapter 2 Literature Review

This literature review aims to provide the necessary background and details for metamaterials and, more specifically, elastodynamic metasurfaces as well as discuss previous work on designing them and how the bandgap has been widened in previous studies.

2.1 Metamaterials

One of the most prevalent features of metamaterials for electromagnetics, optics, and acoustics is their potential ability to manipulate waves in a variety of ways. There have been numerous studies that show various applications and methods for how metamaterials can control wave propagation [9 – 13], but this study will focus on the category of acoustic metamaterials. Deymier describes acoustic metamaterials as "composite structures designed to tailor elastic wave dispersion (i.e. band structure) through Bragg's scattering or local resonances to achieve a range of spectral (ω-space), wave vector (k-space), and phase (ϕ-space) properties" [14]. While Bragg's scattering is a widely used mechanism, which is most often achieved using phononic crystals, for metamaterial design, it requires periodic unit cells with dimensions comparable to the wavelength of the propagating wave. This dependency on the wavelength makes Bragg's scattering impractical for large-wavelength applications. However, local resonance, which relies on using resonators attached to a medium, works through hybridization between the resonances and antiresonances of the resonators and the wave modes propagating through the medium. This makes local resonance a more ideal option for creating compact metamaterial designs that may not necessarily be periodic and can be applied at subwavelength scale, which makes it useful for low-frequency applications.

While metamaterials can be used to control incident wave propagation in a variety of ways such as wave steering [15, 16], mode separation [17], and signal focusing [18], this study will look at metamaterials that are used to suppress incident wave propagation. These types of metamaterials are particularly important for applications requiring vibration isolation such as in surface acoustic wave devices, earthquake protection, or for designing physical filters. In most cases, effective wave suppression often occurs over a short range of frequencies known as a bandgap. Figure 2-1 shows an example of a short bandgap with a bandwidth of approximately 770 Hz. This bandgap is the result of using an acoustic metamaterial created using a chiral phononic crystal [19]. While it is useful to suppress short frequency ranges for more targeted applications, many scenarios, such as those that lack a known incident wave frequency, require increased width of the bandgap to be able to suppress a wider range of frequencies simultaneously. The primary goal of this study is to investigate the bandgap and methods for expanding it for a specific type of acoustic metamaterial and wave propagation.

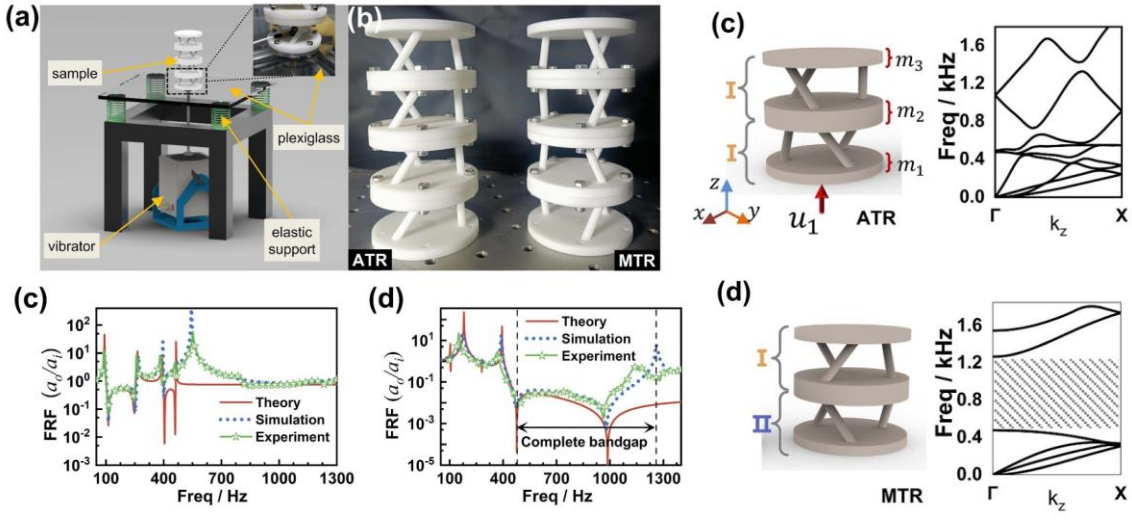

Figure **2-1**: Experimental and numerical results using dispersion curves and the frequency response function to show a bandgap for a metamaterial using chiral phononic crystals [19]

2.1.1 Locally Resonant, Elastodynamic Metasurfaces

This study will focus on a subcategory of acoustic metamaterials called locally resonant, elastodynamic metasurfaces. A metamaterial that consists of resonators coupled to a surface and relies on local resonances is called a locally resonant metasurface. In this case, the resonators are attached to a thin plate, which acts as a waveguide for elastic waves. Being a type of waveguide, incident waves in the plate propagate in the in-plane directions, and the possible fundamental wave modes include the symmetric (S_0), antisymmetric (A_0), and shear-horizontal (SH_0) Lamb waves. For this study, the S_0 Lamb wave mode will be the primary focus. This type of metasurface that is used to control Lamb wave propagation is called an elastodynamic metasurface.

Elastodynamic metasurfaces have been shown to be capable of incident wave suppression. One of the first studies to focus on this type of metamaterial was done by Rupin et al. where a metasurface was created using long, cylindrical rods applied to a thin plate [1]. The study showed, using dispersion curves and frequency spectrum of displacements to determine the bandgaps, that it is possible to control the propagation of the A_0 Lamb wave mode using these resonators glued to the plate (see Figure 2-2). A later study by Williams et al. expanded on this metasurface design by using an analytical theory to model the dispersion that was measured experimentally in the previous study [2]. Using this analytical model, which was based on the hybridization between the flexural and compressional resonances of the resonators with the A_0 Lamb wave mode, they were able to relate the bandgap to a transcendental equation, which could be used to design metasurfaces using rods as resonators. However, this design approach, while effective, is limited to only rod-like resonators. Similarly, the relations mentioned were intended to be used to predict bandgap characteristics, so they may not be appropriate when trying to optimize the design for wider bandgaps.

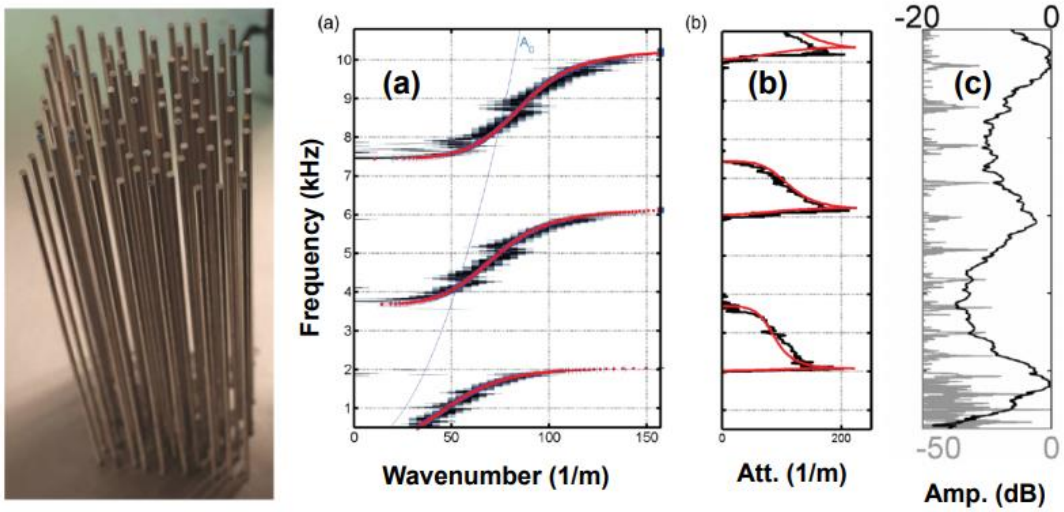

Figure **2-2**: A metasurface consisting of an array of 100 vertical, aluminum rods with a, b) experimental and numerical results for dispersion curves and c) frequency spectrum of horizontal (gray) and vertical (black) displacements measured at the free end of a single rod on a plate [1,2]

Although the frequency response function (FRF) is often mentioned in literature for its inherent use of determining the resonances and antiresonances of a particular resonator, it is rarely used as a tool for determining metasurface characteristics prior to transmission measurements. One exception to this tendency can be seen in the work by Pillarisetti et al. where the FRF is directly compared with the transmission spectra for a metasurface designed to suppress Rayleigh wave propagation, which is a type of surface wave in bulk media [8]. It is shown that the longitudinal and flexural resonances and antiresonances for a single resonator are related to the limits of the bandgap in the metasurface consisting of an array of resonators. Figure 2-3 shows how the resonances align with the lower bounds of the bandgaps while the antiresonances align closely with the upper bounds of the bandgaps. Using this apparent connection between the FRF and the transmission spectrum, it can be implied that changes in the FRF, which only depends on the resonator, is likely to relate to a corresponding change in the transmission spectrum for the full metasurface with an array of resonators on a substrate. Therefore, if a similar connection exists for 2-dimenisonal metasurfaces, then it may be possible to use the FRF

as a basis for the resonator design criterion. Before a design criterion can be established, however, an understanding of the appropriate boundary condition that the resonator needs to approximate when applied to the plate is needed to determine the effect the resonator may have on the substrate.

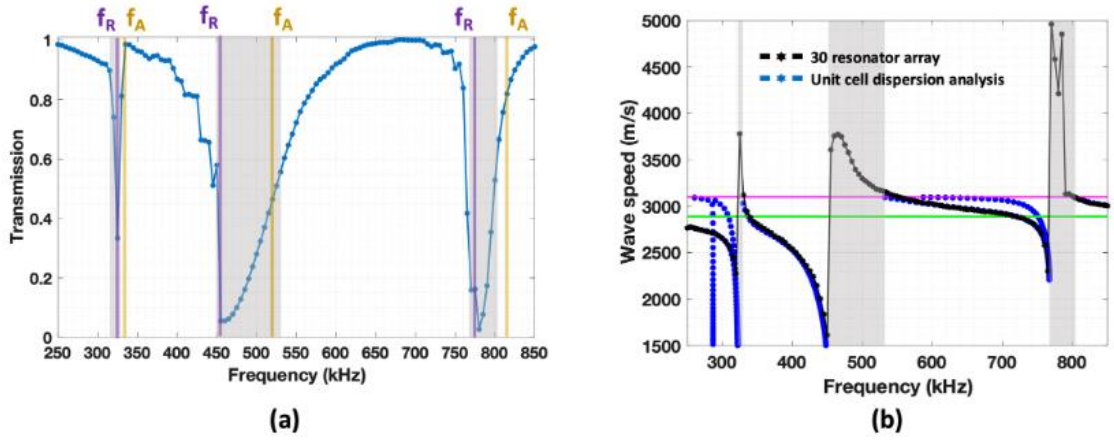

Figure **2-3**: a) Transmission spectrum of an array of 30 prismatic resonators on a simulated half space made from the same aluminum with marked resonances (f_R) and antiresonances (f_A) and highlighted bandgaps observed in b) dispersion curves for a corresponding unit cell [8]

2.1.2 Boundary Conditions

To develop an effective resonator design, it is first important to understand the previously established design criteria for creating locally resonant metasurfaces. Resonators for locally resonant metasurfaces can be designed based on the boundary condition that they apply to the substrate. Hakoda et al. further developed the work first introduced by Rupin et al. and Williams et al. to also show the viability of using a similar approach for resonators meant to suppress the S_0 Lamb wave mode [3]. The study further goes into describing the "clamping" boundary condition that the resonators have on the plate. This method of designing resonators, which resulted in a 4-arm resonator design as shown in Figure 2-4, that apply this type of boundary condition was shown to be particularly effective for suppressing the S_0 Lamb wave mode whereas only

frequency matching was necessary for the A_0 mode in previous studies. The "clamping" effect was best shown at the resonator's antiresonances, which could be tuned to a desired frequency. Lissenden et al. further investigated this boundary condition approach by comparing Frequency-Domain Finite Element (FDFE) models of thin strips of aluminum with either a coupled clamping 4-arm resonator or an applied boundary condition patch that covers the same area [4]. The study also used the wavenumber spectrum to determine the transmission of the S_0 Lamb wave mode at 50 kHz, which corresponds to a wavenumber of 58.7 rad/m for a 1 mm aluminum plate. However, it is often necessary to be able to suppress more than a single frequency at one time, which would require a wider bandgap.

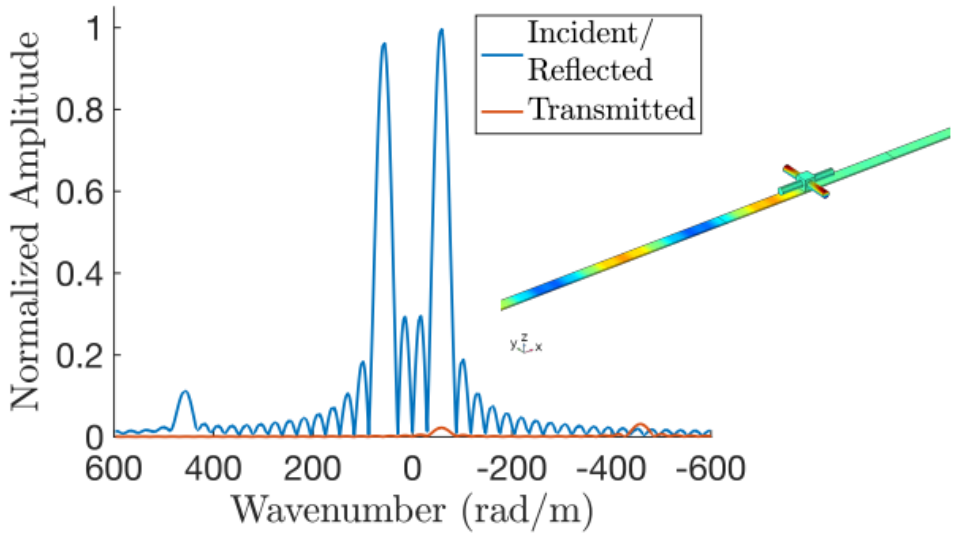

Figure **2-4**: Wavenumber spectra for incident and transmitted regions of a thin strip with a single 4-arm resonator coupled to the surface [4]

2.2 Bandgap Widening

The bandgap for locally resonant metasurfaces can be widened in a variety of ways. One method for increasing the width of the bandgap is to simply increase the number of resonators in the array. The increased number of resonators covers more surface area on the substrate. Therefore, the boundary condition is enforced over a larger area, which has a limited widening effect on the bandgap [5, 20]. More complex methods for enhancing the bandgap might include trying to reinforce existing resonances of the resonators by strategically adding holes to the plate [21], by introducing disorder in the system to promote localization of the eigenmodes of the frequency bands [22] or by combining both Bragg scattering and local resonance effects to cause each individual bandgap to overlap and create an overall wider bandgap [23]. While these approaches were shown to be effective, the simplicity of the resonator geometry in each case is a potential limiting factor. This same limiting factor is one of the main issues with a more common approach for widening the bandgap called resonator grading.

2.2.1 Resonator Grading

Resonator grading works by designing individual resonators to cover different frequency ranges and combining them into one array to create a wider bandgap than the individual resonators would in a similar array consisting of only a single resonator geometry. However, this often requires an iterative approach to the resonator design process and limits resonator designs to only those that are easily tunable to work at different frequencies. Many studies focus on determining resonator geometries whose target frequency can be easily tuned based on trial and error by changing certain geometric values [5, 7, 20, 24]. This grading approach is commonly referred to as “rainbow trapping.” One example of this approach uses Legos to create a

"rainbow" metamaterial where pillars are used as resonators with varying heights for a small mass on each pillar [6]. Figure 2-5 shows how the experiment was set up and how the transmission spectra vary with each arrangement. Each color in the transmission spectra represents the bandgap when using a single resonator geometry, which are labelled from T to M5. The overlapping of all the bandgaps together when combined in a single resonator arrangement clearly results in a wider final bandgap for the overall metasurface.

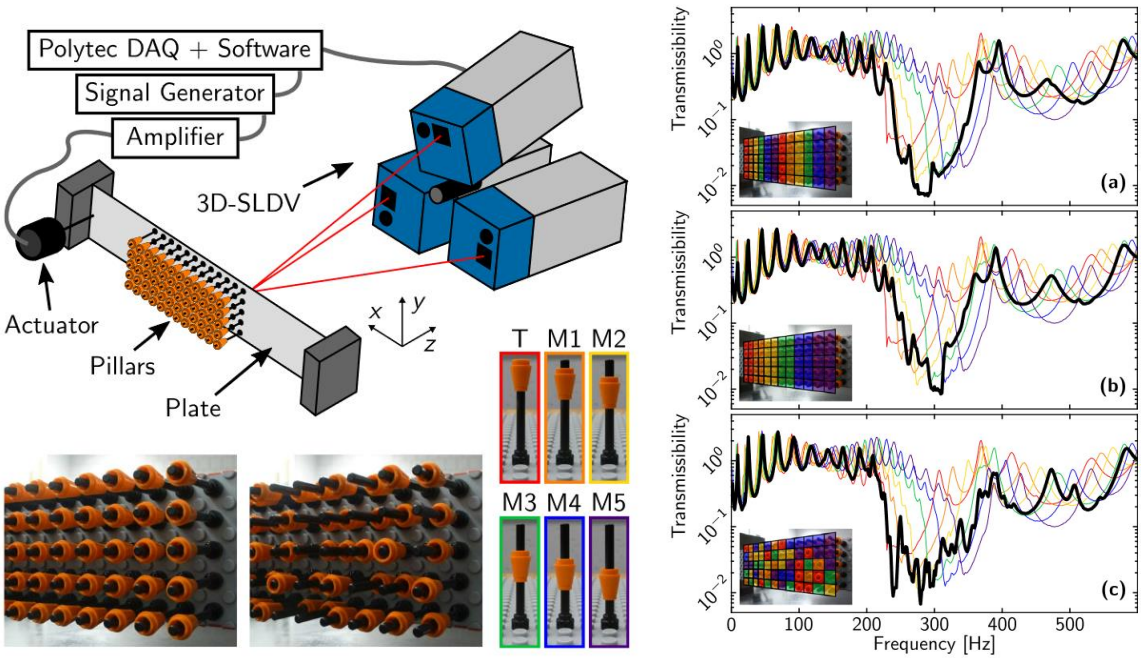

Figure **2-5**: Experimental setup for a graded resonator arrangement on a plastic plate for both a and b) order arrangements and c) a disordered arrangement of pillar-like resonators [6]

While resonator grading has been shown to be an effective method for widening the bandgap, there are limitations. One such limitation is that the resonator geometries are often simple, intuitive designs that are easily tunable to the desired target frequency. Prismatic or pillar-like resonators are some of the most used shapes for these resonators because of their simple geometry where only one or two dimensions need to be changed to alter the target frequency of each resonator. Their simple shape also allows for close spacing in the metasurface

array, which is a beneficial characteristic when using their local resonances [1]. Another limitation for resonator grading is the lack of a singular design methodology for getting the desired metasurface characteristics. The most common approach is simply trial and error of designing resonators, testing their frequencies and transmission, and then redesigning appropriately to get the desired target frequencies. Analytical models have been developed for simple resonator designs, such as the rod-like resonators [2], but it is desirable to have an approach that may be used to develop new, less-intuitive resonator geometries.

A potentially better approach may involve creating resonators that result in naturally wide bandgaps in the metasurface. Such resonators would not require being tuned to individual frequencies because a single resonator design would be enough to cover the necessary bandwidth. Additionally, metasurfaces with only a single resonator design are potentially more robust and have more opportunities for redundancy in the design to ensure that the desired effect is achieved. An efficient rational methodology is lacking in this approach, but topology optimization has already shown some promise in being used for metasurface design and may be the type of methodology that is missing.

2.3 Topology Optimization

Topology optimization has been steadily growing in popularity as a viable design approach in recent years. Topology optimization is a type of design methodology that uses one of many possible algorithms to selectively iterate a structural design based on an objective function [25]. The characteristics defined in the objective function drive the process to produce a structure that preferentially enforces a predefined condition. With improvements in computational power and more efficient methodologies, topology optimization is proving to be capable of being useful in a variety of fields. In the field of metasurfaces, this is of particular interest because there is a

possibility of using a topology optimization approach for designing nonintuitive resonators instead of being limited to mostly resonators that have analytical solutions or otherwise simple, easily tunable characteristics.

2.3.1 Resonator Design

Before trying to optimize the bandgap, it is important to understand how a topology optimization for locally resonant metasurfaces would work. Topology optimization has already been shown by Giraldo et al. to be used for designing resonators that impose an appropriate clamping boundary condition for use in locally resonant, elastodynamic metasurfaces [26]. These resonators, as shown in Figure 2-6, can be used to suppress the S_0 Lamb wave mode when attached to the surface of a thin plate made from the same material. The topology optimization used to generate these resonators uses a density-based approach to either remove or add material within a finite domain. With each iteration of the optimization, the FRF is calculated, and the antiresonances are identified. The objective function is defined such that the optimization attempts to create a resonator with an antiresonance around 50 kHz when under excitation at the base that is meant to approximate the motion of the S_0 Lamb wave mode. In doing so, the resonators are designed to have a bandgap around 50 kHz. This bandgap, however, is shown to be narrow, so a different optimization is needed to create resonators that result in wider bandgaps for the metasurface.

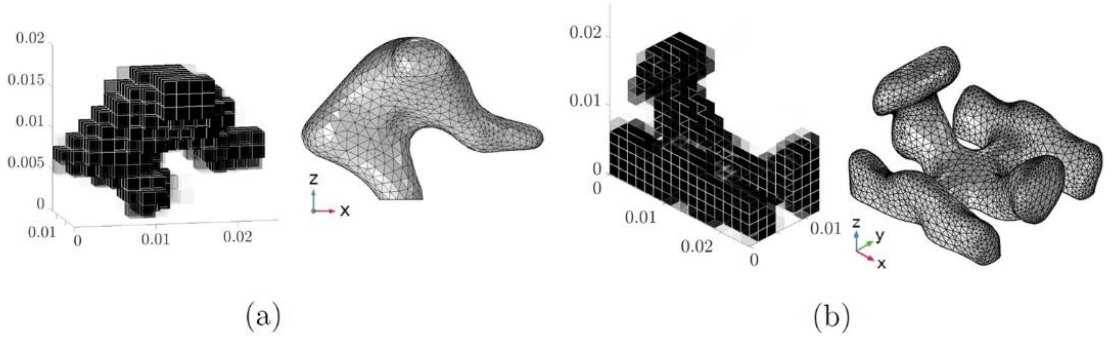

Figure **2-6**: Topology-optimized resonators designed to control S_0 Lamb waves with raw topologies on the left and post-processed topologies on the left for a) an elephant-like topology and b) a boat-like topology [26]

2.3.2 Optimization for Bandgap Widening

Many previous studies rely on dispersion analysis to determine bandgaps and motivate topology optimization. A study by Jung et al. shows how the topology optimization based on simulated annealing can be used to generate resonators that tailor flexural bandgaps in plates [27]. A reduced Bloch mode expansion is used to simplify dispersion analysis for calculating the bandgap, which is defined as the difference between the lowest and highest eigenvalues on the upper and lower bands respectively (see Figure 2-7). This simplification is noted to be necessary to reduce the number of function evaluations that are required to iterate the optimization algorithm using dispersion analysis. Similarly, the resonator geometry is limited to being a plate-like shape centered on a single support. This approach was able to increase the bandgap by more than 100% between the first and final iterations of the optimization. However, the limited 2-dimensional resonator geometry is potentially problematic when attempting to increase the bandgap further, which would likely require extending the optimization domain to three dimensions.

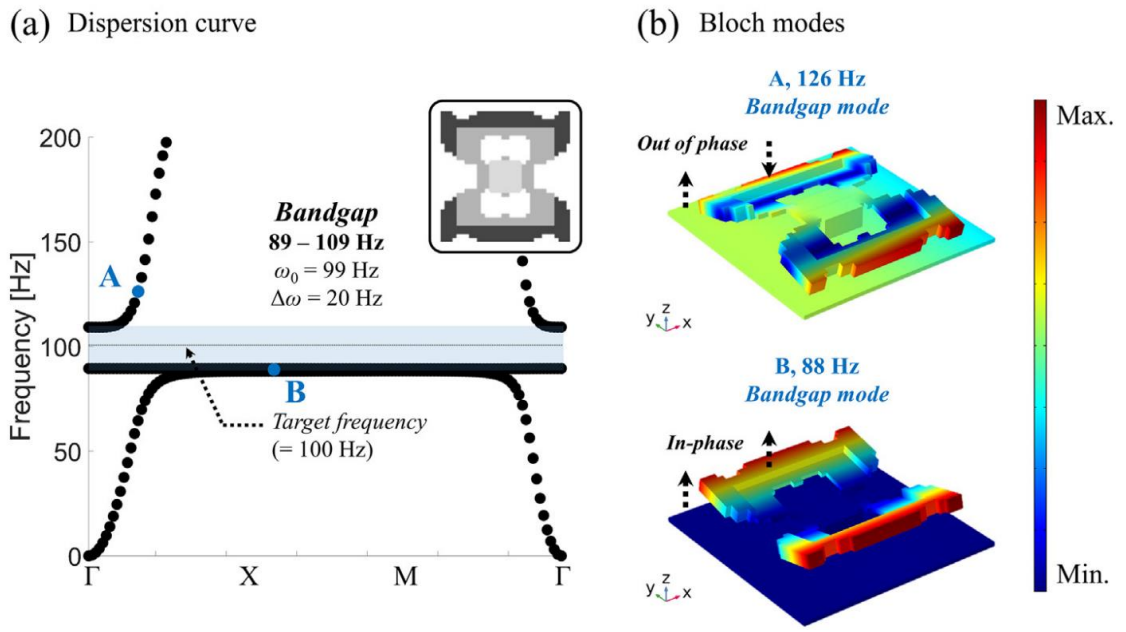

Figure **2-7**: a) Dispersion curves for a topology-optimizedresonator with highlighted bandgap and b) Bloch mode shapes at points A and B [27]

Other studies use similar methods by changing the waveguide geometry itself [28,29]. These studies suffer from the same limiting factors related to the required simplifications of the optimization problem to make the process more computationally feasible and counteract the numerical inefficiency of using dispersion analysis to calculate the bandgap for each iteration. This project aims to show that, if the goal is to use local resonances to create the bandgap, then dispersion analysis is not needed and a simpler motivation for topology optimization may be used instead.

2.4 Knowledge Gaps

Although successful locally resonant metasurfaces have been developed using various techniques and criteria, the existing methods are mostly limited to simple resonator geometries.

Furthermore, there is a lack of a rational methodology that is widely applicable. This gap is especially true when attempting to design a metasurface for broadband applications. One potential option for developing such a methodology may involve the use of topology optimization for creating an appropriate resonator that can be used to create a metasurface with a wide bandgap. To be able to use topology optimization, a motivating parameter first needs to be determined. This parameter would need to be computationally feasible for repeated calculations in the optimization process as well as intuitive for understanding how to create an appropriate objective function for the optimization to evaluate the quality of each iteration. This study aims to justify that the resonances and antiresonances as calculated in the FRF may be used as the necessary parameter for motivating the optimization. Previous studies found a possible connection between the FRF and the bandgaps in the transmission spectra for locally resonant metasurfaces for surface waves in bulk media, but a similar connection has yet to be presented for other wave modes or media. The S_0 Lamb wave mode in thin plates has proven to be an appealing option for this study because of its well-understood properties and intuitive particle motion. The existence of many previous studies using simple, prismatic resonators to suppress this wave mode is also beneficial for creating a reference to compare with a topology-optimized resonator.

Chapter 3 Numerical Methods

This study primarily focused on using a variety of numerical methods to evaluate the performance of metasurfaces constructed using resonators of different geometries. COMSOL Multiphysics 6.1 was used to run finite element simulations to generate frequency response functions, dispersion curves, and wave-structures. It was also used to run frequency-domain finite element (FDFE) simulations of the metasurface that were used to numerically determine transmission spectra. Results of these simulations are then processed in MATLAB for plotting and analysis.

3.1 Frequency Response Function

The frequency response function (FRF) is defined as the displacement averaged over the traction-free base of a resonator. To calculate the FRF, a single resonator was subjected to a frequency-varying harmonic excitation at its base in the x-direction, which coincides with the horizontal direction in the model shown in Figure 3-1. The horizontal forcing approximates the particle motion on the surface of a plate when excited by S_0 Lamb waves. The resulting displacement components (u, v, w measured along the x, y, and z-directions) at the base of the resonator are then surface averaged for each excitation frequency. The magnitudes of these components are plotted separately because it is expected that the u-component, which is measured along the x-direction, would have the most direct connection to the bandgap for the S_0 mode. Given that their range spans multiple orders of magnitude, the calculated average displacements are plotted on a logarithmic scale against frequency (on a linear scale). The frequencies where the displacement is a local maximum indicate resonances while the frequencies

where the displacement is a local minimum are known as antiresonances. Therefore, the frequency response function provides a useful visual representation of the resonances and antiresonances, which can be compared with the bandgaps when the resonator is mounted on the waveguide and the bandgaps seen in the dispersion curves.

Figure 3-2 shows the frequency response function for an aluminum (Young's Modulus = 70 GPa, Poisson's Ratio = 0.33, and Density = 2700 kg/m^3) prismatic resonator that is 23.39 mm tall and has a 7.86 mm x 7.86 mm base. These dimensions correspond to a physical sample having an aspect ratio greater than three. For the u-component, the antiresonances appeared at 41.5 and 102 kHz and the resonances at 57 and 115.5 kHz as shown in Figure 3-2. Having an antiresonance higher than 40 kHz, this resonator met a criterion for future experiments.

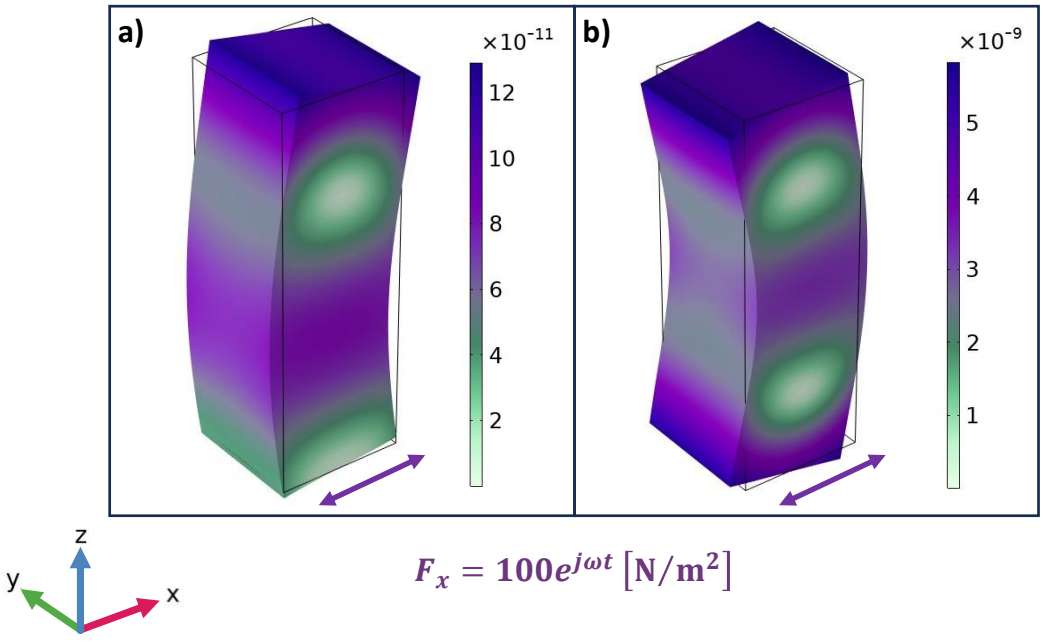

Figure **3-1**: Displacement magnitude of a prismatic resonator under harmonic, horizontal excitation at the base in the x-direction for a) the antiresonance at 41.5 kHz and b) the resonance at 57 kHz

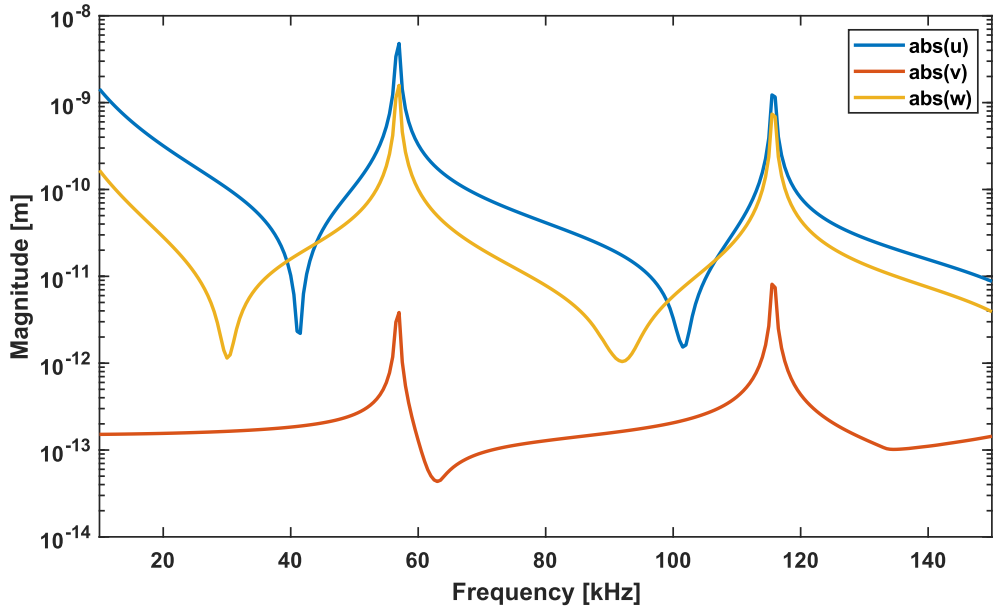

Figure **3-2**: Frequency response function taken at the base of a prismatic resonator and divided into the u, v, and w components or x, y, and z respectively

3.2 Dispersion Analysis

Dispersion curves were used to identify the modes of the resonator mounted on the waveguide by considering the metasurface unit cell assuming an infinite periodic resonator arrangement. Dispersion analysis is also useful for predicting where the bandgaps would occur [30] and for generating the wave-structure through the thickness of an aluminum plate. An advantage of this analysis is that it reveals all possible modes of the metasurface unit cell consisting of the resonator coupled to the plate. However, dispersion analysis is not computationally efficient and requires manual filtering to clearly identify the bandgaps and remove evanescent modes that do not propagate in the plate.

The dispersion curves were computed using an eigenfrequency study in COMSOL considering a unit cell consisting of a single prismatic resonator coupled to an 11 mm x 11 mm square portion of the 1-mm plate. Bloch-Floquet continuity conditions are applied to the plate on

the two face pairs perpendicular to the in-plane direction. The irreducible Brillouin zone is defined by the edges of the plate, but only the x-direction portion of the analysis was considered because it matches the direction of wave propagation. The wavenumber is normalized based on the size of the irreducible Brillouin zone, and the volume-averaged displacement components in the plate are exported for each point in the dispersion curves (see Figure 3-3). The complex displacement components are separated to exclude any modes with primarily v-component motion, which are not the modes propagating in the metasurface subjected to incident S_0 Lamb waves. Excluding the v-component, the relative motion between the u and w-components can be calculated as follows:

$$\frac{|w|^2}{|u|^2 + |w|^2} \tag{3-1}$$

In Equation 3-1, if the u-component is the dominant motion (for example, in the S_0 mode in the plate or flexural modes in the resonator), the value of the equation will be small, closer to zero. Similarly, if the w-component is the dominant motion (for example, in the A_0 mode in the plate or longitudinal modes in the resonator), the value of Equation 3-1 will be closer to one. Therefore, using this equation helps to distinguish the flexural modes from the longitudinal modes of the resonator by using the displacement seen in the plate.

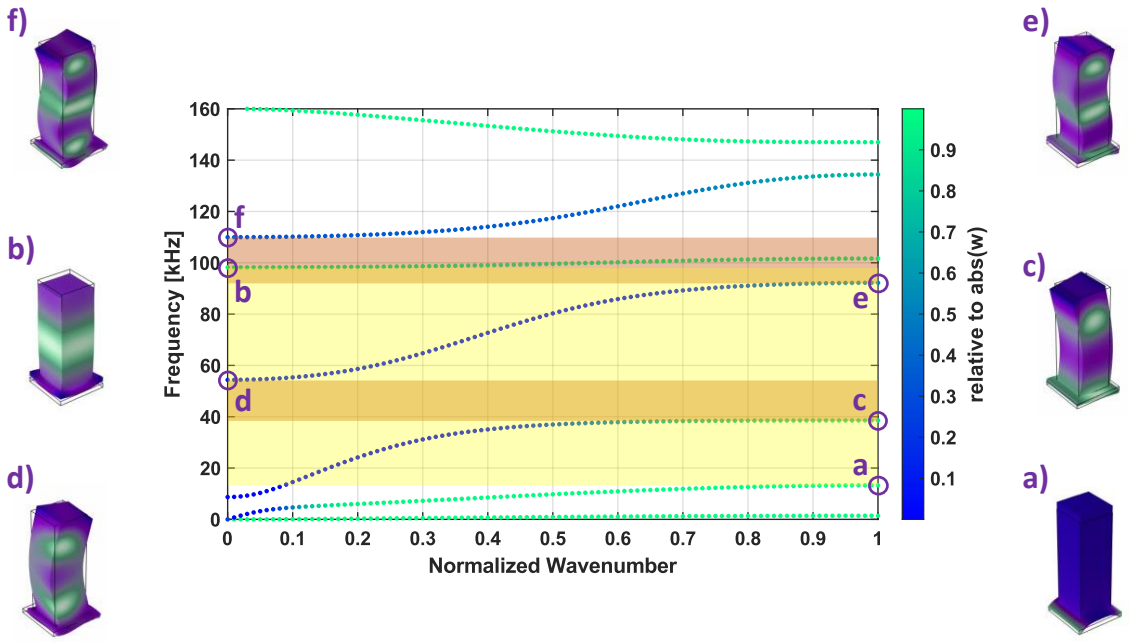

Figure **3-3**: This figure shows dispersion curves for a 23.39 mm x 7.86 mm x 7.86 mm prismatic resonator on an 11 mm x 11-mm plate to create the unit cell. The value of Equation 3-1 is indicated by the color bar and the longitudinal (a, b) and flexural (c, d, e, f) modes of the resonator are labelled at their respective frequency and wavenumber pairs. Bandgaps for both A_0 (from a to b) and S_0 (from c to d and e to f) modes are highlighted.

3.2.1 Mode Shapes

One application of the dispersion curves is to identify modes of the resonators such as the flexural and longitudinal modes (see Figure 3-3). Each frequency and wavenumber pair on the dispersion curve corresponds to a mode shape that can be visualized in COMSOL. These 3D mode shapes show the distribution of maximum displacements in the resonator, and therefore, they are useful for identifying the type of motion the resonator would experience at each frequency. In our study, the flexural modes were of particular interest because those would be the modes corresponding to the resonator exerting a clamping effect on the plate during S_0 Lamb wave propagation [3]. The gap between separate flexural modes would determine the predicted bandgap for the resonators. For example, the orange-shaded regions (38.5 kHz to 54.4 kHz and

92.2 kHz to 110.0 kHz) in Figure 3-3 show where the S_0 bandgap is expected for the prismatic resonator because they mark the gap between successive flexural modes. Similarly, the yellow-shaded region (13.3 kHz to 98.2 kHz) shows where the A_0 bandgap is expected between successive longitudinal modes.

3.2.2 Wave-Structure Generation

By computing the dispersion curves for the 1-mm plate, the wave-structure within the plate could be calculated and used for defining a body-load excitation in COMSOL that preferentially excites the forward-propagating S_0 Lamb wave mode. The wave-structure is the stress profile through the thickness of the plate. Each point in the dispersion curves is associated with a unique wave-structure, and these values can be extracted once the appropriate mode is identified (see Figure 3-4). This means that the stresses that define the wave-structure for that mode can be extracted by using the values at each point in that line.

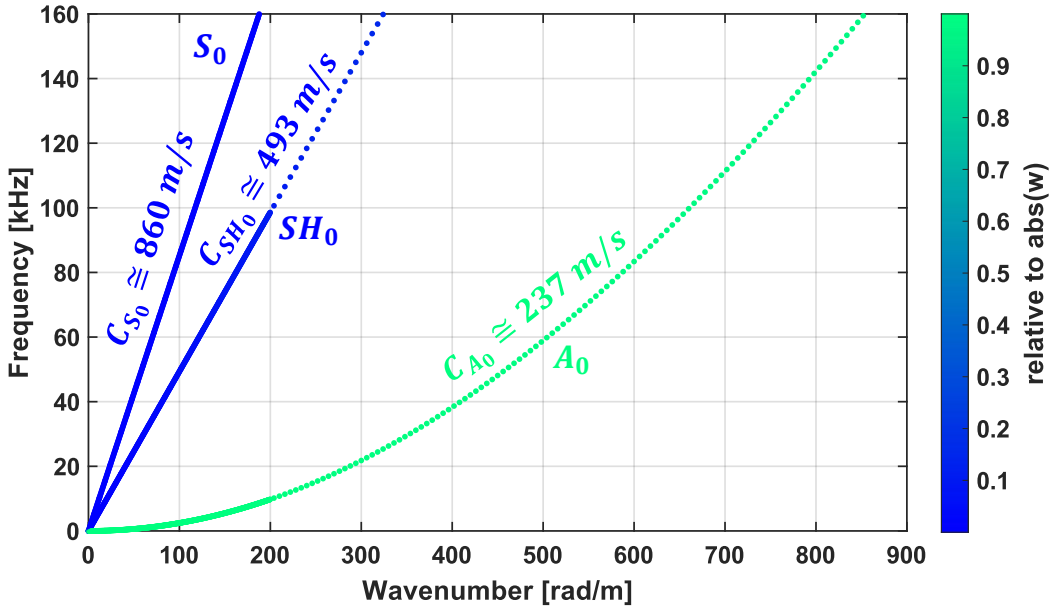

Figure **3-4**: Dispersion curves for a 1-mm plate showing the first three fundamental Lamb wave modes with approximate wave speeds at 50 kHz labelled

To calculate the wave-structure, a 70 μm x 70 μm section of the 1-mm plate is considered as shown in Figure 3-5. The size of the section of 1-mm plate is directly related to the range of wavenumbers that can be calculated for the dispersion curves. Larger plate sections reduce the maximum wavenumber that can be calculated, so a small section is needed to represent the full frequency range up to 160 kHz for all three fundamental modes. The dispersion analysis is conducted as previously described and the resulting dispersion curves are plotted in Figure 3-4. Using the dispersion curves, the S_0 and A_0 Lamb wave modes can be identified by their slopes, which corresponds to the wave speed of each mode. The S_0 mode propagates faster than the other two fundamental modes below 160 kHz, so it has a larger slope by comparison (see Figure 3-4). Additionally, the value of Equation 3-1 for the A_0 mode should be close to one, as its primary particle motion is in the z-direction. Once the mode of each line is identified, the corresponding set of eigenfrequencies can be selected. A cut line is used through the center of the model to extract stress values through the thickness of the plate. For each point in the dispersion curve, the real and imaginary parts of all six unique stress components are computed separately along the cut line. These stresses are then used to define the loading for pure S_0 mode excitation.

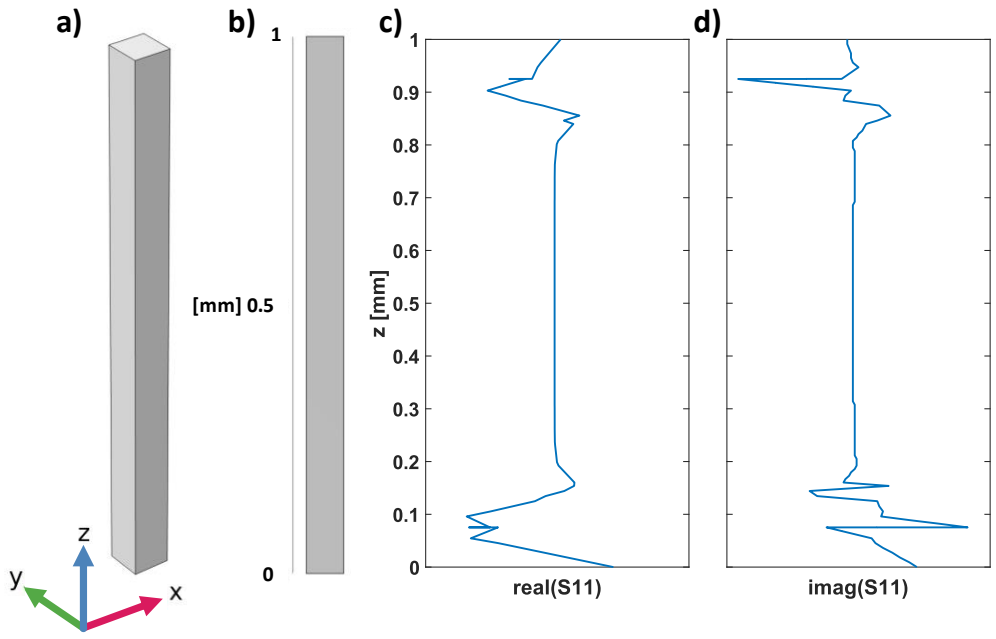

Figure **3-5**: Wave-structure example showing a) an isometric view of the 70 µm x 70 µm section of the 1-mm plate, b) a side view of the plate section, c) the real s11, and d) the imaginary s11 wave-structure stresses at 41.458 kHz through the thickness

3.3 FDFE Metasurface Model

The metasurface is defined as the plate with resonators fully attached to the surface. In this study, both the resonators and the 1-mm plate are made of aluminum and are therefore assumed to have the same material properties. For example, simple metasurface designs were modelled in COMSOL Multiphysics using dimensions of the prismatic resonators in multiple arrangements on the plate. A baseline model with just the plate was also created. The baseline models serve as the reference and allow for investigation of the metasurface performance and calculation of a transmission ratio for each metasurface considered. To model the metasurfaces, an appropriate meshing methodology was also developed to ensure the accuracy of the reported results.

3.3.1 Design

The model consists of an aluminum plate that is 150 mm wide in the y-direction and 1 mm in the z-direction. The plate is surrounded by perfectly matched layers (PMLs) to prevent reflections off the edges (see Figure 3-6). This is to ensure that the finite plate model behaves approximately like an infinite plate without requiring very large dimensions to be meshed, which would increase the computational cost of the numerical simulations.

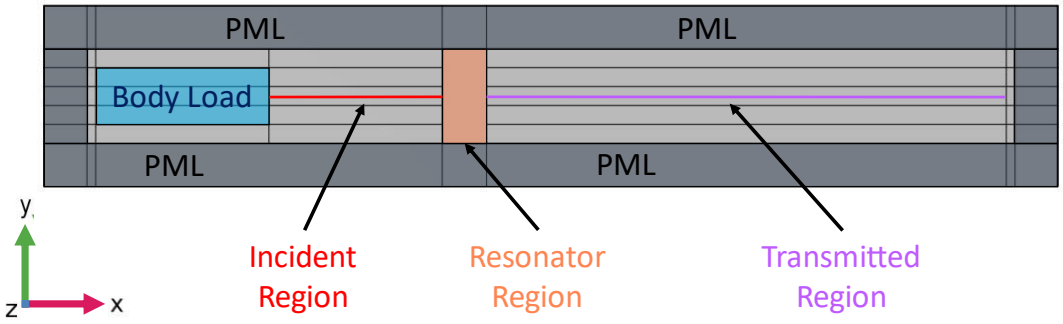

Figure **3-6**: Schematic showing the baseline COMSOL plate model

In the x-direction, the plate is divided into regions called buffer, loading, incident, resonator, transmitted, and another buffer. The buffer regions allow space to prevent the loading and transmitted regions from being in contact with the surrounding PML region, which may cause numerical errors. The loading region is defined to have a body load with components that use the generated wave-structures as an input to create a pure S0 mode excitation (see Equations 3-2 to 3-5). The equations to use the stresses as the input to a forcing function are as follows:

$$F_x = \left((S11(z) + S12(z) + S13(z))e^{-jkx}\right)10^{-3} \quad \textbf{(3-2)}$$

$$F_y = \left((S22(z) + S12(z) + S23(z))e^{-jkx}\right)10^{-3} \quad \textbf{(3-3)}$$

$$F_z = \left((S33(z) + S13(z) + S23(z))e^{-jkx}\right)10^{-3} \quad \textbf{(3-4)}$$

$$S11(z) = real(S11)(z) + j * imag(S11)(z) \quad \textbf{(3-5)}$$

where $S11(z), S22(z), S33(z), S12(z), S13(z),$ and $S23(z)$ are the stress profiles, divided into their real and imaginary components as shown in Equation 3-5, through the thickness of the plate in the z-direction. A body load was used in favor of a line load definition because the body load enables a full wavelength of the S_0 mode to be the excitation across the loading region. This loading helps to enforce the forward propagating pure mode generation by adding the phase information to the input signal. A line load would simply apply the excitation along a surface through the thickness of the plate, which would lack phase information and result in both forward and backward propagating modes in the plate.

To minimize the size of the model, x-dimensions are dependent on the frequency of the excitation. Specifically, the size of the plate changes based on the wavelength of the S_0 mode propagating through it. Each simulation was altered to include the frequency-dependence using MATLAB LiveLink (see Appendix A). Each region was defined by a minimum number of wavelengths to fit within them in the x-direction, which was the direction of wave propagation, to ensure that the excited signal is well-represented on the length scale of the model. This is especially important for the transmitted region where data will be exported from later. Therefore, the size of each region is determined based on the number of wavelengths of the S_0 mode because it is the mode with the largest wavelength of the fundamental modes for a given excitation frequency between 20 kHz and 150 kHz. Other modes with smaller wavelengths that may appear as part of the interactions with the resonators would fit within the minimum wavelength requirement. The loading region is determined to be at least one wavelength to ensure that the S_0 mode is fully enforced. Similarly, the incident region is also one wavelength to allow the excitation to develop and ensure plane waves at the beginning of the resonator region, which negates the need to consider any other incidence angle of the wave on the resonator region other than normal. The resonator region dimensions are arbitrarily set to be 70 mm in the direction of wave propagation to have enough space to fit the resonator arrangements. The transmitted region

is defined to have at least four wavelengths to allow enough distance to define a cut line on the surface along the center of the region, as seen in Figure 3-6, from which to extract the displacements for use in post-processing. The two buffer regions are set to 0.05 wavelengths to allow space between the PMLs, the body load, and transmitted region. The PMLs were tested at numerous wavelengths, but 0.25 wavelengths were ultimately chosen for preventing reflections while being small enough to not significantly increase the number of elements in the mesh.

3.3.2 Mesh

The mesh for the metasurface model was determined based on the expected modes in the plate. Namely, the maximum element size is based on the minimum wavelength of expected possible modes because the smallest wavelength requires a sufficiently small element size to accurately represent the wave. Therefore, the mesh of the plate needed to be based on the A0 mode because it represents the smallest wavelength that the plate could experience for a given frequency. Additionally, an overall maximum element size is determined to ensure that the element size is still comparable to the thickness of the plate.

A convergence study was conducted to validate the chosen meshing parameters. As shown in Table 3-1, five iterations of meshing parameters were conducted at 85.3 kHz (wavelengths for the S_0 and A_0 modes respectively are λ_{S_0} = 62.8 mm and λ_{A_0} = 10.4 mm), which is approximately the center frequency in the range of interest. Column 4 in Table 3-1 shows the optimal meshing parameters used for all FDFE simulations. The maximum element size for quadratic elements in the plate was determined to be at most seven times smaller than the minimum wavelength with an overall maximum of 1 mm. Similarly, the maximum element size for tetrahedral elements in the resonator region is at most ten times smaller than the minimum wavelength with an overall maximum of 1.5 mm. Figure 3-7 shows a sample of the mesh for the

largest wavelength case where the tetrahedral elements can be clearly distinguished from the surrounding quadratic elements. Figure 3-8 shows the convergence of displacement normalized to the maximum value at each point over the 5 iterations considered in Table 3-1.

Table **3-1**: Meshing parameters used in the 5 iterations of the convergence study with highlighted column indicating meshing parameters chosen for all FDFE simulations

Mesh Parameters	**1**	**2**	**3**	**4**	**5**
Total Elements	119578	248024	533489	1062018	1675419
Maximum Element Size (Plate)	$\frac{\lambda_{A_0}}{1} \leq 5$ mm	$\frac{\lambda_{A_0}}{3} \leq 3$ mm	$\frac{\lambda_{A_0}}{5} \leq 2$ mm	$\frac{\lambda_{A_0}}{7} \leq 1$ mm	$\frac{\lambda_{A_0}}{8} \leq 0.75$ mm
Minimum Element Size (Plate)	$\frac{\lambda_{A_0}}{2} \leq 1$ mm	$\frac{\lambda_{A_0}}{4} \leq 1$ mm	$\frac{\lambda_{A_0}}{6} \leq 1$ mm	$\frac{\lambda_{A_0}}{8} \leq 0.5$ mm	$\frac{\lambda_{A_0}}{9} \leq 0.25$ mm
Maximum Element Size (Resonators)	$\frac{\lambda_{A_0}}{4} \leq 5$ mm	$\frac{\lambda_{A_0}}{6} \leq 4$ mm	$\frac{\lambda_{A_0}}{8} \leq 3$ mm	$\frac{\lambda_{A_0}}{10} \leq 1.5$ mm	$\frac{\lambda_{A_0}}{11} \leq 1$ mm
Minimum Element Size (Resonators)	$\frac{\lambda_{A_0}}{5} \leq 1$ mm	$\frac{\lambda_{A_0}}{8} \leq 1$ mm	$\frac{\lambda_{A_0}}{10} \leq 1$ mm	$\frac{\lambda_{A_0}}{12} \leq 1$ mm	$\frac{\lambda_{A_0}}{13} \leq 0.5$ mm
Maximum Element Growth Rate	1.5	1.5	1.5	1.5	1.5
Curvature Factor	0.6	0.6	0.6	0.6	0.6
Resolution of Narrow Regions	0.5	0.5	0.5	0.5	0.5

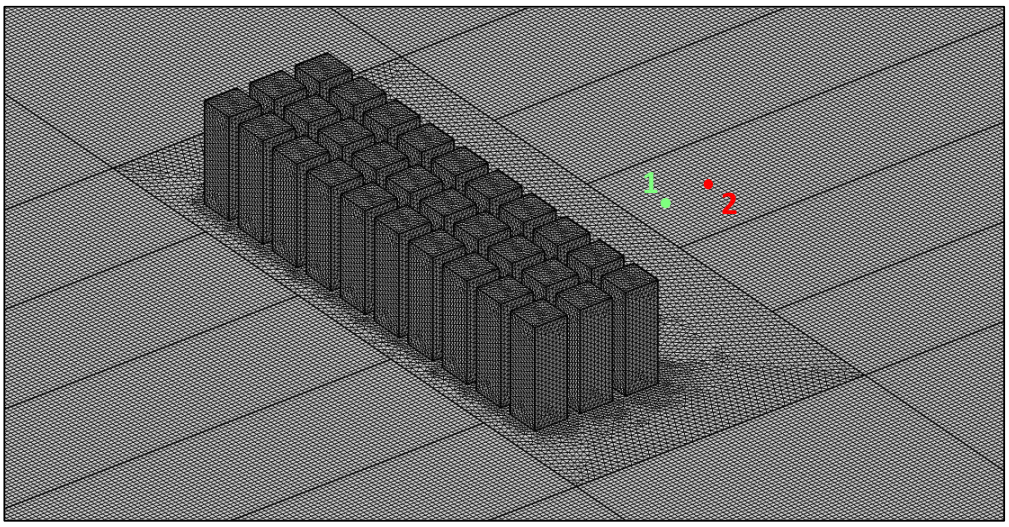

Figure **3-7**: Example mesh for prismatic resonators at the largest wavelength at 19.5 kHz with points 1 and 2 indicating where displacements were taken for showing result convergence with successive iterations of finer meshing

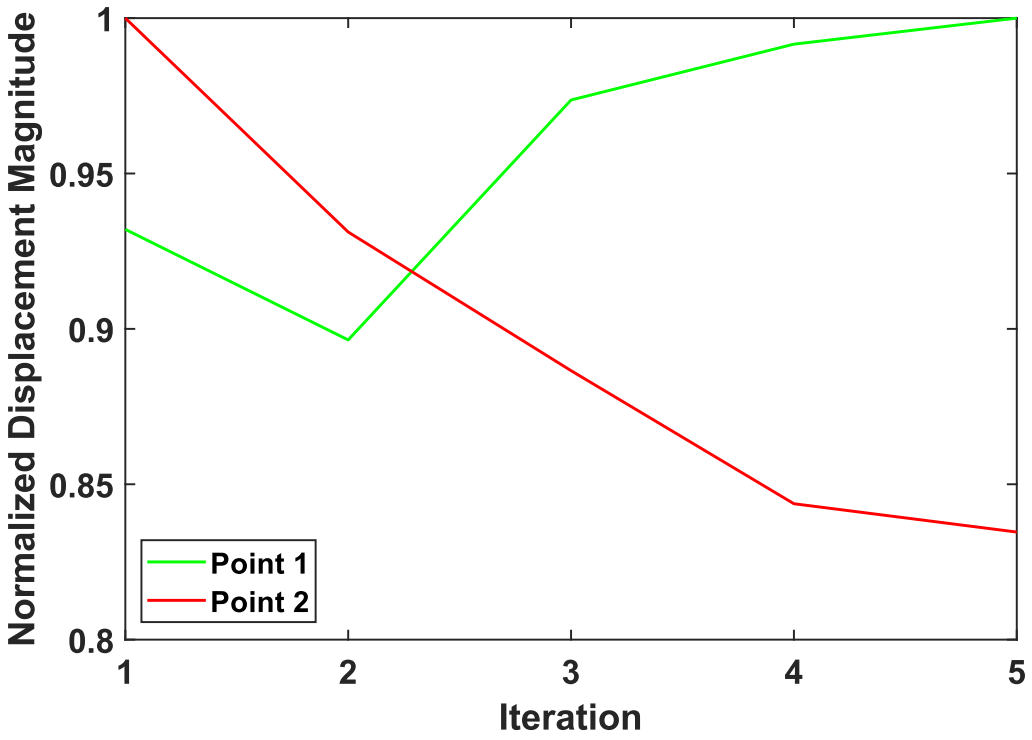

Figure **3-8**: Normalized displacement magnitude showing convergence for successive iterations of finer meshing as indicated in Table 3-1 in the convergence study

3.3.3 Resonator Arrangements

The different resonator geometries were arranged in a variety of ways within the resonator region depending on the size and shape of each resonator. Based on previous studies, it is expected that the resonators would work best when placed in tightly packed arrangements to prevent energy leakage between the resonators [1,5]. Therefore, both in-line and staggered arrangements were considered to minimize space between resonators. Figure 3-9 shows the two primary arrangements that were considered. The first arrangement shows thirty in-line prismatic resonators arranged in three rows of ten. The second arrangement shows sixteen prismatic resonators in an off-center, staggered pattern. The larger dimensions of the staggered arrangement match the arrangement that will be used to minimize spacing for a later resonator

topology and will provide a better comparison between the two resonator geometries. Additionally, a baseline case is calculated by using the same plate with no resonators in the resonator region. This baseline was then used to normalize the transmission results in post-processing.

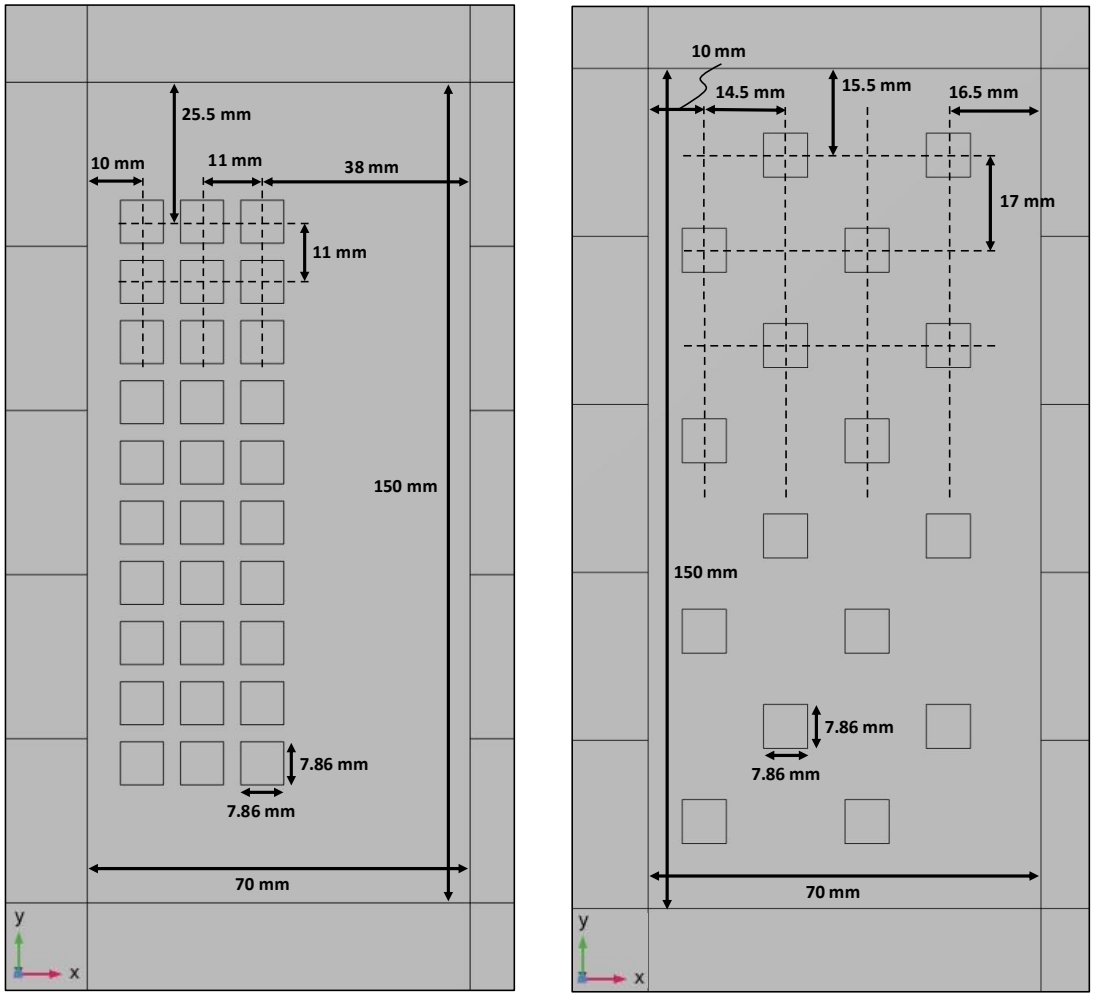

Figure **3-9**: Schematics showing the dimensions for the 10x3 and 4x4ocs arrangements of resonators

3.4 Post-Processing

After the displacements along the cut line in the transmitted region are exported from COMSOL, they are saved in a text file for each frequency to be read in MATLAB. These values are then used to calculate the spatial fast Fourier transforms (FFTs) at each frequency, which generates the corresponding wavenumber spectra.

3.4.1 Spatial Fast Fourier Transform

A spatial fast Fourier transform was used to convert the displacements along the cut line to signal amplitude for each wavenumber. This calculation results in a plot of the wavenumber spectrum, which shows how much transmitted signal there is at each wavenumber (see Figure 3-10). In these plots, positive and negative wavenumbers are determined based on the direction that the displacements are ordered in the calculation. Taking the displacements starting at the edge of the resonator region and ending at the edge of the buffer region results in negative wavenumbers corresponding to waves propagating in the positive x-direction. As mentioned previously, the body load excitation includes phase information, so only forward propagating (i.e. in the positive x-direction) S_0 Lamb waves should be excited. Similarly, the PML regions should prevent any backward propagating waves in the transmitted region. As seen in Figure 3-10 for the baseline simulation, both conditions result in a single peak in the wavenumber spectrum at a negative wavenumber with a magnitude that matches the wavenumber for the S_0 mode at the defined excitation frequency.

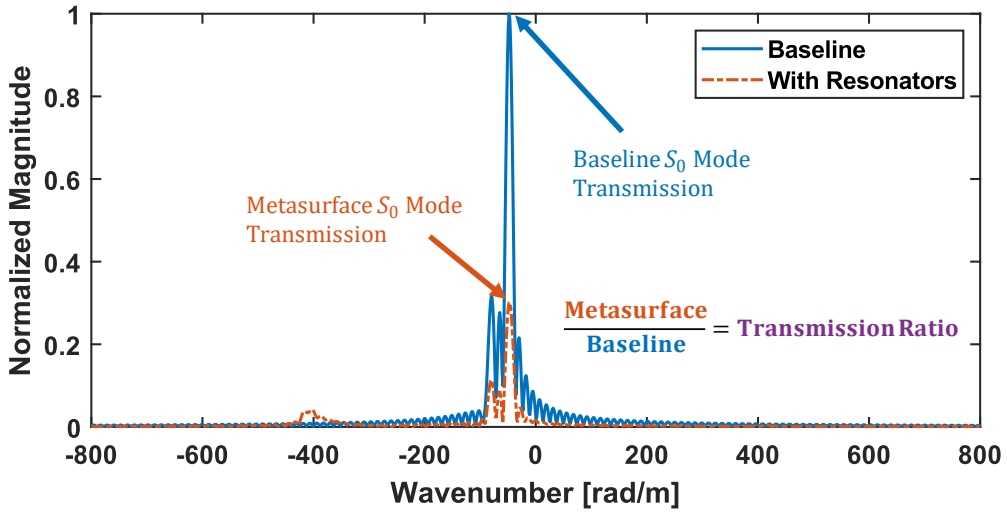

Figure **3-10**: Wavenumber spectrum from transmission region of metasurface with 10x3 arrangement of prismatic resonators at 41.458 kHz

From the dispersion curves of the 1mm plate (see Figure 3-4), it is known what mode corresponds to each wavenumber, so it can be verified that a pure mode is being excited in the baseline simulation. For example, the wavenumber for the S_0 mode at 41.458 kHz is approximately 48.64 rad/m, which matches with the magnitude of the wavenumber at which there is a peak as seen in Figure 3-10.

3.4.2 Transmission Spectra

Using the wavenumber spectra, the transmission of S_0 mode Lamb waves can be determined by using the signal amplitude at the corresponding wavenumber. A ratio was taken at the desired wavenumber between the signal amplitude from the transmitted region of a metasurface for each resonator geometry and the signal amplitude from the baseline simulation without resonators. The resulting value shows how much of the S_0 mode was transmitted compared to the baseline without resonators. This means that values less than one correspond to

a drop in transmission due to the application of the resonators. This process is repeated at each calculated frequency to get a plot of the transmission spectrum across a range of frequencies from 20 kHz to 150 kHz. An example of the transmission spectrum for the prismatic resonator in the 10x3 arrangement can be found in Figure 3-11.

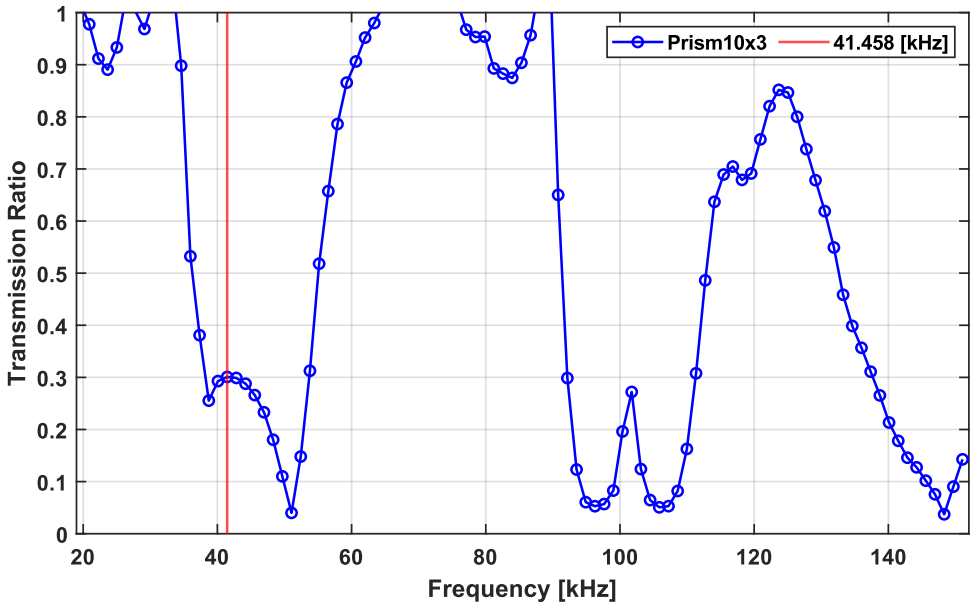

Figure **3-11**: Transmission spectrum for a 10x3 arrangement of prismatic resonators with the frequency 41.458 kHz indicated by a vertical line to match the wavenumber spectrum shown in Figure 3-10

Chapter 4 Experimental Methods

A series of experiments were conducted to verify transmission results from the COMSOL simulations for prismatic resonators. A sample 1 mm aluminum plate is used along with prefabricated prismatic resonators cut from an extruded rod of aluminum with the same dimensions as previously reported in the numerical methods. The setup for these experiments was developed to yield accurate data while still being relatively simple to allow taking multiple iterations of measurements. A data acquisition system was used to produce the excitation and take measurements on the plate both with and without the resonators attached. The experimental data was then processed in MATLAB to calculate the 2-dimensional fast Fourier transform (2D FFT) and create dispersion planes and the transmission spectra.

4.1 Metasurface

The metasurface consists of a 1000 mm x 510 mm region of a 1 mm thick aluminum plate and an array of aluminum, prismatic resonators that are attached to the surface of the plate using Loctite super glue (see Figure 4-1). The region is surrounded by an 11 mm boundary made from duct sealing putty. The putty is about 2 to 4 mm thick around the plate, and it is meant to reduce backwall reflections from the edges of the plate outside of the defined region. The array of prismatic resonators is centered on the plate in the 510 mm dimension, and the first row of resonators was placed 400 mm away from the transducer (see Figure 4-2). The 10 x 3 resonator array is arranged to match the dimensions used in the numerical simulations. The resonators were also measured, and the average dimensions match the prismatic resonators in the previously

reported COMSOL simulations with a standard deviation of ±0.05 mm for the height and ±0.02 mm for the base dimensions.

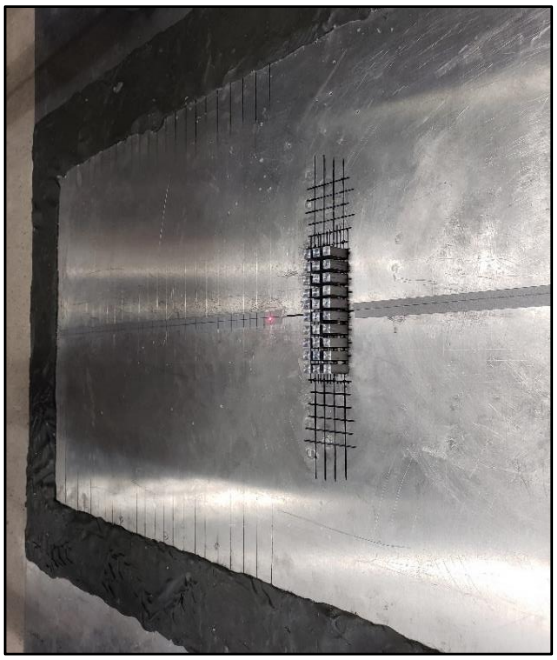

Figure **4-1**: The metasurface with a duct putty barrier around the edges to reduce edge reflections made from a 1-mm aluminum plate and aluminum, prismatic resonators

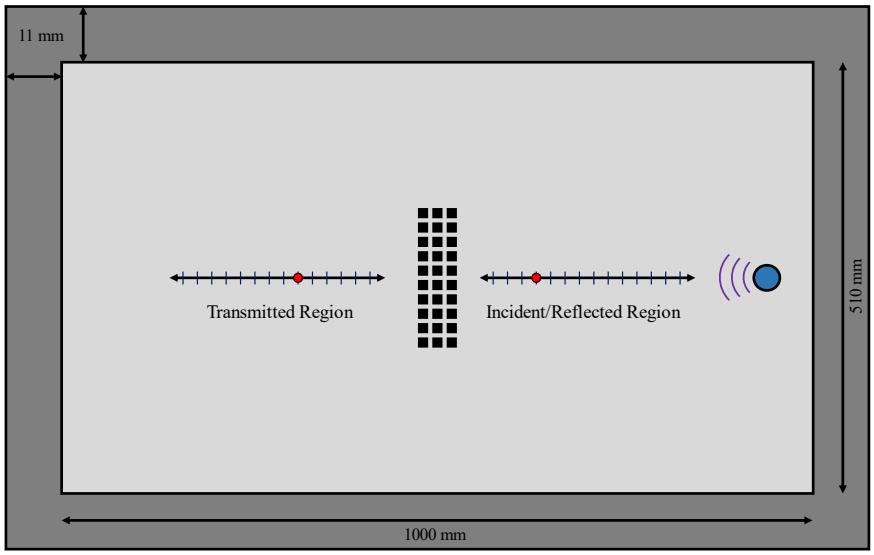

Figure **4-2**: Schematic of the metasurface used for the experiments showing the incident/reflected and transmitted regions along with the transducer placement with labelled dimensions of the plate

4.2 Setup

The experimental setup consists of a data acquisition system with corresponding signal flow, and a scanning stage that was used to take consistent measurements over the transmission region.

4.2.1 Transducers and Data Acquisition System

The data acquisition system allows generation of the incident wave and reception of the response. Figure 4-3 shows the equipment that makes up the data acquisition system. The desired settings for the signal generator (f_s = 500 MHz, V = 1 V_{pp}, number of pulses = 100, repetition interval = 0.01 s) and oscilloscope (f_s = 50 MHz, record time = 1000 s, input impedance = 50, range = 5 V_{pp}) are input into the computer through a Python script (see Appendix B). The signal generator (80 MHz 16-bit AWG) is set to produce a 3-cycle, harmonic pulse with a Hanning window for the excitation signal. The generated signal passes through a TEGAM High Voltage Amplifier, with amplification set to 50x fixed gain. The amplified signal is input to an Olympus 1.0-inch, 100 kHz S-wave Transducer (V1548). This transducer is adhered to the plate using about a tablespoon of melted phenyl salicylate, also known as salol. To provide a static load as the salol solidifies, a weight is immediately placed on top of the transducer after it is placed in the melted salol. The transducer is then checked to ensure it is properly aligned to the center of the plate and that enough salol was used to surround the transducer and uniformly cover the contact surface. The salol is let to cool for about 5 minutes before measurements can begin because the salol needs to fully solidify for signal amplitude to converge and remain stable. The response is recorded in either the transmitted or incident regions using a laser doppler vibrometer (LDV) consisting of a Polytec OFV-505 Sensor Head and

Polytec OFV-5000 Vibrometer Controller. The LDV is set at an angle of approximately 34° from vertical to capture both in-plane and out-of-plane motion of the plate surface (see Figure 4-4). The LDV signal is sent through a pre-amplifier (Olympus 5077PR) with a gain set to +20 dB before going to the 100 MHz Oscilloscope to be recorded and sent to the computer for saving. Figure 4-5 shows the full signal flow of the data acquisition system used for the experiment.

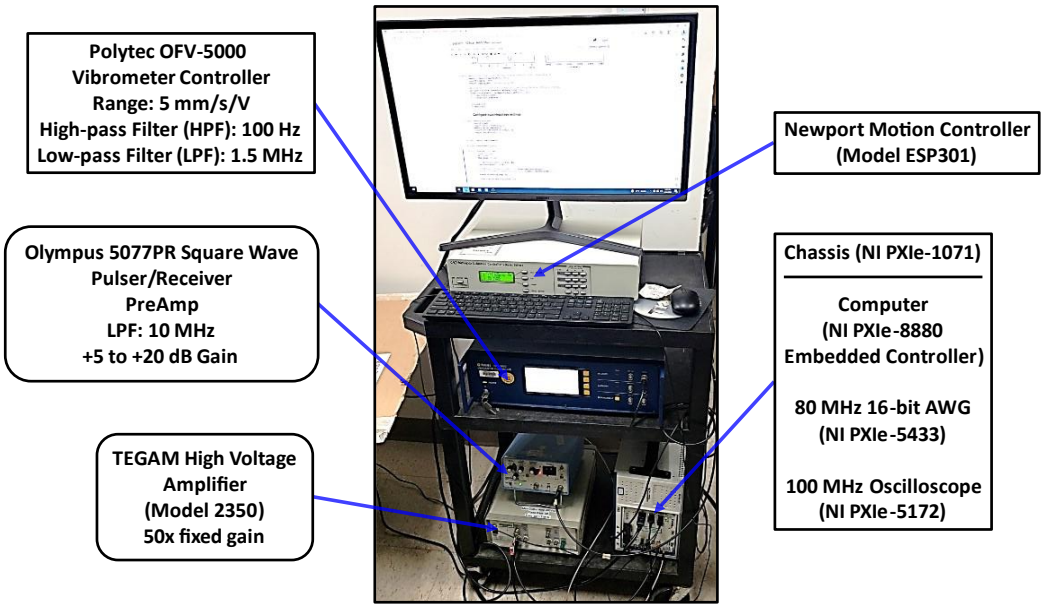

Figure **4-3**: Data acquisition system with labelled components

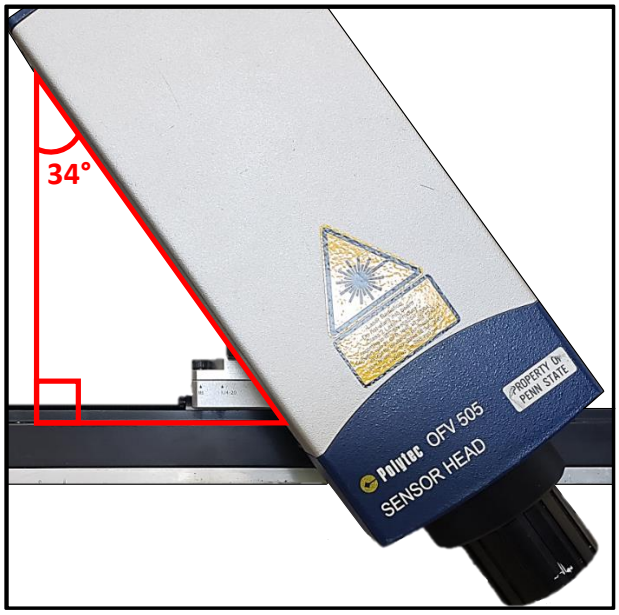

Figure **4-4**: Laser Doppler Vibrometer (LDV) pointed at reflective tape in the transmitted region of the plate and angled 34° from vertical to measure both in-plane and out-of-plane velocities

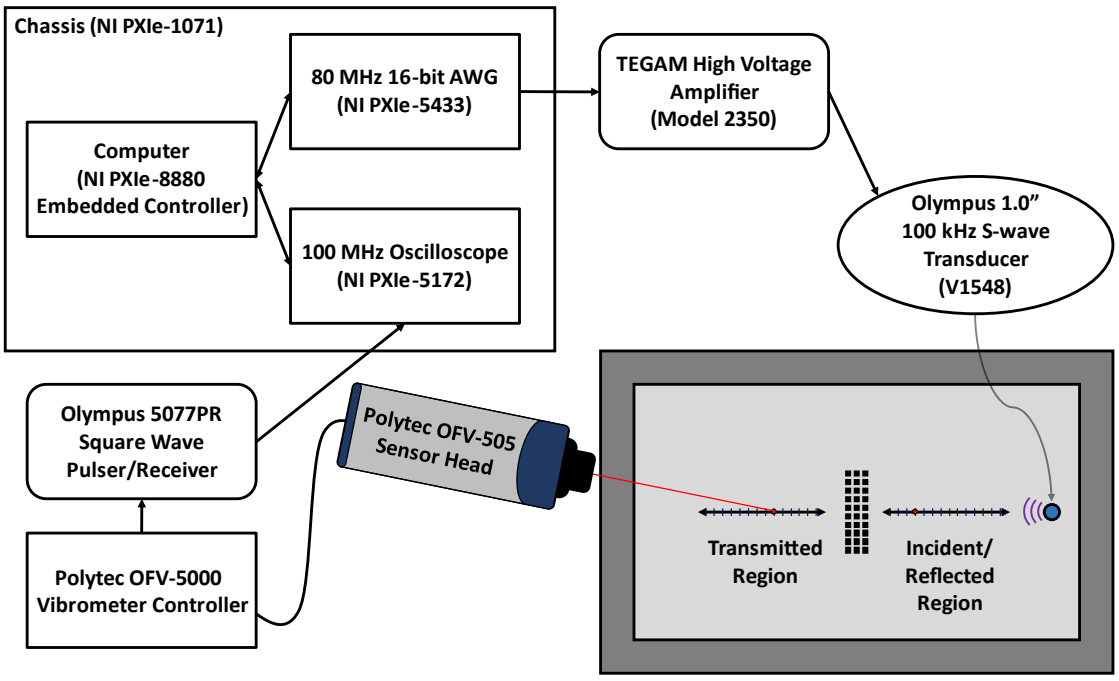

Figure **4-5**: Signal flow of the experimental setup showing the usage of each component in signal generation in the incident/reflected region and reception in the transmitted region of the plate

4.2.2 Scanning

To increase the repeatability of the recorded A-scans, a Newport scanning stage (ILS250PP) was used to control the movement of the LDV. The stage and LDV are mounted to a cart such that the lens of the LDV sits approximately 540 mm above the floor (see Figure 4-6). The stage moves the LDV in 5 mm increments along the length of either the transmission or incident regions. Each region was defined as 250 mm long with the transmitted region starting about 490 mm away from the transducer and the incident region starting about 125 mm from the transducer (see Figure 4-2). Additionally, reflective tape was adhered to the plate in these regions to improve the signal amplitude for the LDV (see Figure 4-1), and the autofocusing feature of the vibrometer controller was used whenever the signal was not strong and stable or a minimum of once every 5 measurements. The scanning stage is controlled using a Newport Motion Controller (Model ESP301), and commands are sent to the controller through the computer using a Python script developed by Lalith Sai Srinivas Pillarisetti. The stage moves on command once it is confirmed that the signal is sufficient, and each new measurement is recorded.

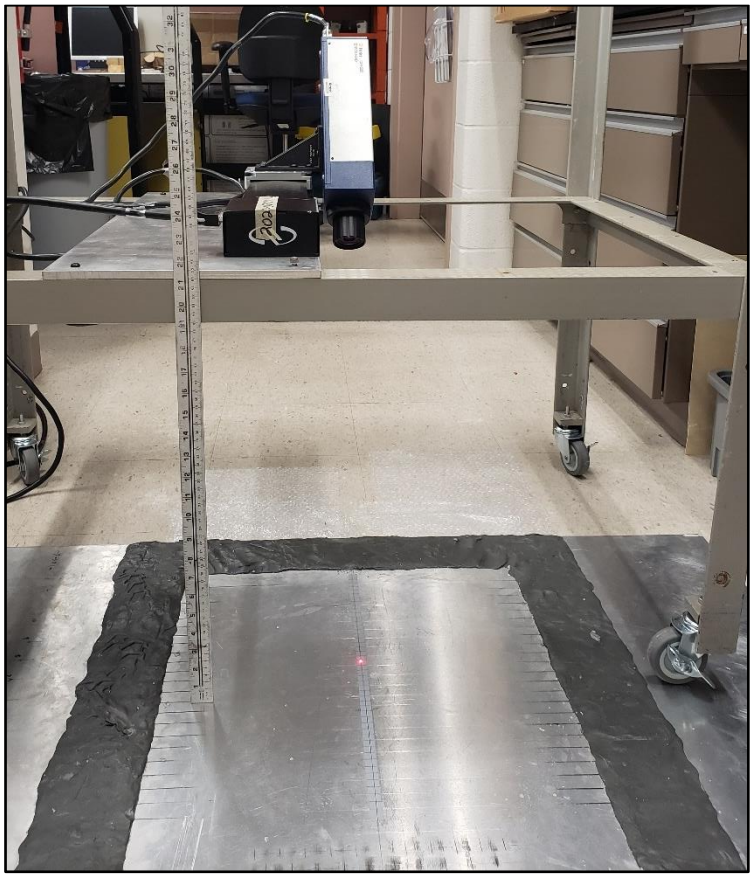

Figure **4-6**: LDV and Newport scanning stage as shown above the transmitted region of the aluminum plate

4.3 Data Processing

After taking measurements along both the transmitted and incident regions for the desired frequencies, the measured data is then processed using MATLAB for calculating the 2-dimensional fast Fourier transform and plotting the transmission spectra.

4.3.1 2-Dimensional Fast Fourier Transform

The first tool used to visualize the results from the data is the 2-dimensional fast Fourier transform (2D FFT). This method involves taking the FFT along both temporal and spatial

dimensions of the data. Each measured data set is a 1000 µs record in the time domain that was taken at a given location along the 250 mm transmitted region, which gives the time and space dimensions respectively. The resulting dispersion plane is a plot of frequency vs. wavenumber with a colormap showing the spectral amplitude of each point.

To get the dispersion planes, a waterfall plot of the recorded signals is used to visualize the signal. The S_0 mode has the highest wave speed and arrives first, so it is easily visible before 200 µs in this view as seen in Figure 4-7a. The signals are then trimmed to remove later modes (see Figure 4-7b). When the 2D FFT is taken using the trimmed signals, it produces a cleaner plot of the spectral amplitude for the S_0 mode. Figure 4-8a shows how the untrimmed data produces spectra that have a high A_0 mode signal and how that compares to the spectra in Figure 4-8b created using the trimmed data to focus on the S_0 mode. The clean plot of spectral amplitude for the S_0 mode is then used to determine the transmission of the metasurface in a similar way to what was done for the numerical analysis.

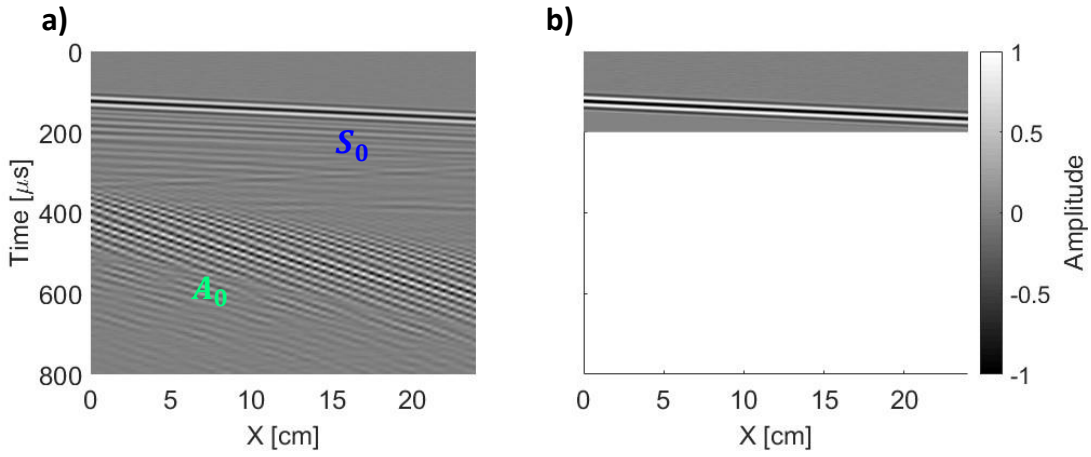

Figure **4-7**: a) the untrimmed and b) trimmed waterfall plots of the recorded signals along the 25 cm transmitted region for the baseline at 50 kHz

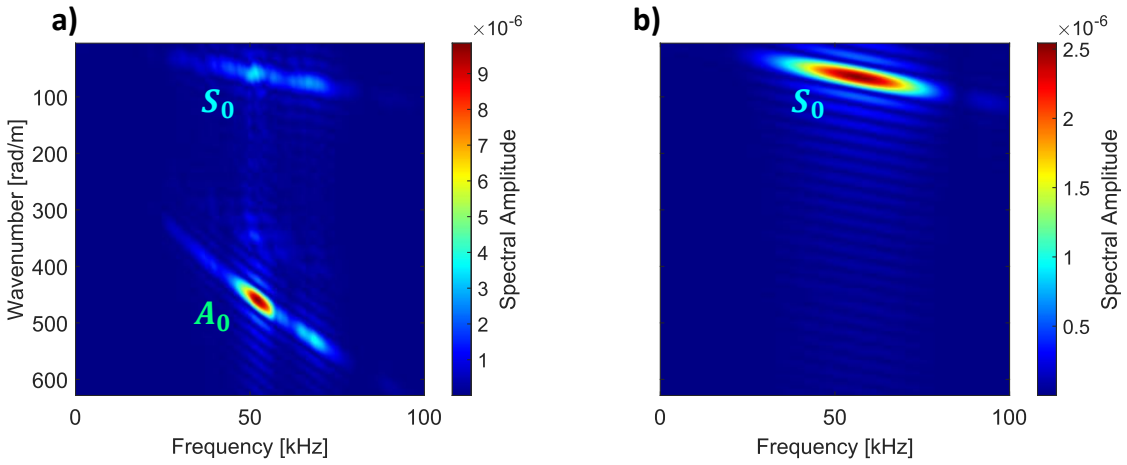

Figure **4-8**: a) the original and b) clean spectral amplitude plots after doing the 2D FFT for the transmitted region in the baseline at 50 kHz

4.3.2 Transmission

Transmission is calculated using the 2D FFT by taking the maximum spectral amplitude values within a range around where the S_0 Lamb wave mode is expected and taking the ratio between the maximum values at each frequency in the metasurface measurements to the maximum values at the same frequency for a baseline measurement, which was taken without any resonators on the plate. Figure 4-9 shows how the maximum spectral amplitude appears through the center of the S_0 mode, which is isolated between an upper and lower boundary, as a black line. The baseline shows what the response would be without resonators, so the transmission shows how much amplitude loss there is due to the resonators compared to when no resonators

are on the plate (see Figure 4-10).

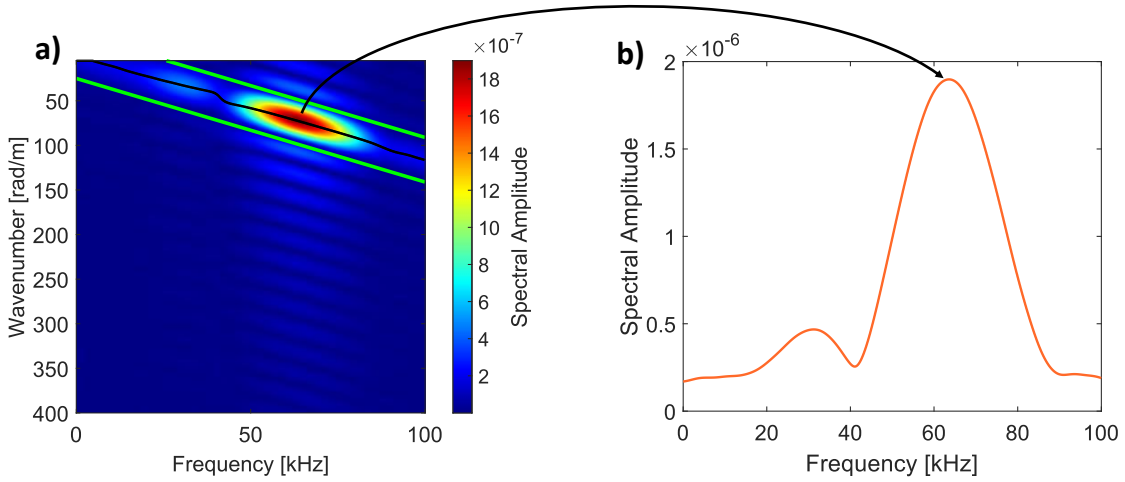

Figure **4-9**: Plots showing the isolated S_0 mode in a) the spectral amplitude plot and b) the maximum spectral amplitude through the S_0 mode for a 10x3 arrangement of prismatic resonators

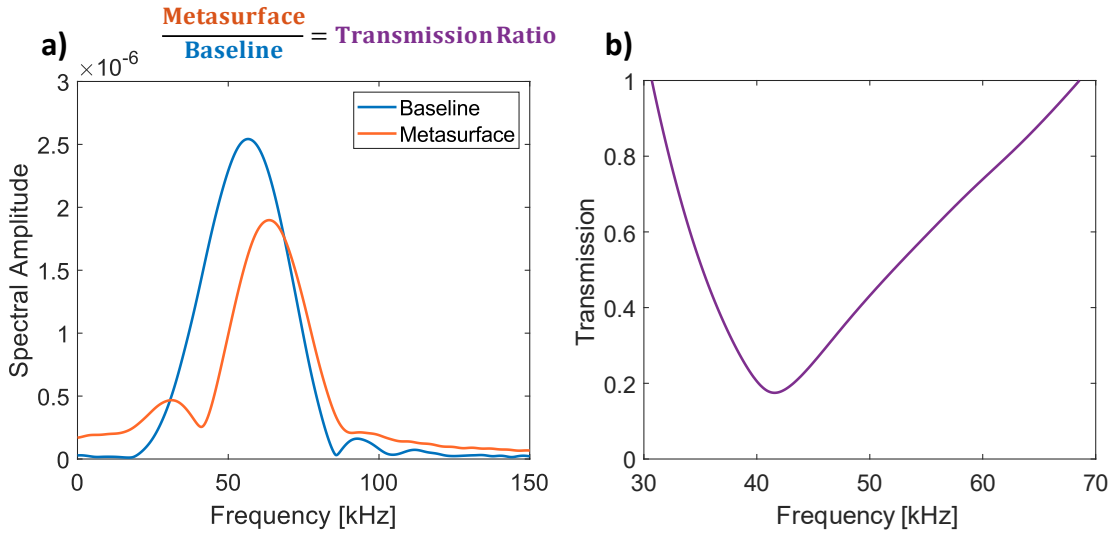

Figure **4-10**: a) the maximum spectral amplitudes compared between baseline and a metasurface with a 10x3 arrangement of prismatic resonators under 50 kHz excitation and b) the calculated transmission ratio using the spectral amplitudes

Chapter 5 Prismatic Resonator Results and Discussion

Using the dispersion curves as a guide, both the simulations and the experiments using prismatic resonators show good agreement on where the bandgaps are in the transmission spectra. However, it is also clear that the arrangement influences the transmission, especially for higher frequencies. Regardless, a connection can be seen between the frequency response function of the resonator and the transmission spectrum of the metasurface created using the resonators.

5.1 Prismatic Resonator

From the dispersion curves for the prismatic resonator, there are two clear bandgaps for the S_0 mode that are below 150 kHz. The first bandgap is between approximately 38.5 kHz and 54.5 kHz, and the second is between 92 kHz and 110 kHz (see Figure 5-1). It is expected that the bandgaps for the metasurface with the 10x3 arrangement should match very closely with these predictions from the dispersion curves because of the simple geometry of the resonator and because the unit cell used in the dispersion analysis matches exactly with the dimensions used in the metasurface for that arrangement. As seen in Figure 3-3, there is an additional longitudinal mode that occurs at 101.7 kHz, which explains the small peak at that frequency in the middle of the higher bandgap (see Figure 5-1). There is some vertical displacement from the S_0 mode due to bulging of the material as the wave passes through, so it is reasonable to say that the additional mode might cause a small change in the expected transmission spectrum. Figure 5-1 also shows how the dispersion curve bandgaps line up with the metasurface bandgap as calculated in the numerical simulations and in the experiments for the same arrangement of resonators. These results validate the numerical methods as well as establish the idea that there are additional

factors to consider beyond the frequency response function, such as additional hybridized modes that appear at frequencies within the bandgap due to the resonator being coupled to the plate.

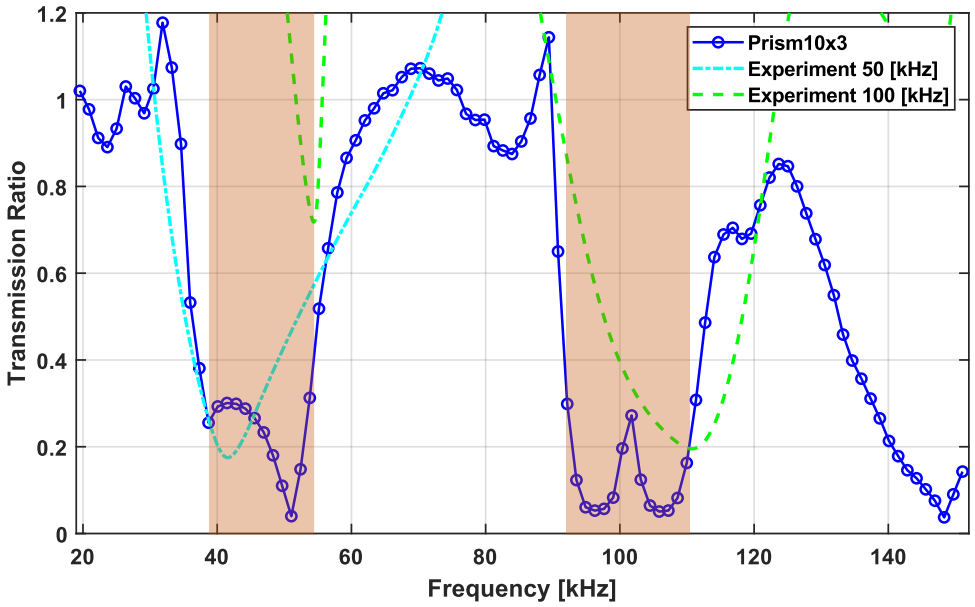

Figure **5-1**: Transmission spectra from numerical and experimental results for a metasurface with 10x3 arrangement of prismatic resonators with highlighted dispersion analysis bandgaps

Although the agreement of these results is a promising observation, it is expected that there would be slight changes in the bandgap when using different arrangements of resonators. Additionally, another arrangement of prismatic resonators that matches the arrangement used for the topology-optimized resonators would provide a better comparison between the resonators because it is known that the total number of resonators can influence the width of the bandgap [5].

5.1.1 Different Arrangements

An additional arrangement was considered using the prismatic resonator where the resonators were no longer in-line, and the spacing was increased to match the arrangement used

later for the resonator generated from topology optimization, which needed to be different because of the dimensions of the topology-optimized resonator (see Figure 3-8). As seen in Figure 5-2, the second arrangement is particularly different in the higher bandgap. Having the higher bandgap shift more than the lower one is likely a result of the increased lattice size (i.e. spacing between the resonators). For the 4x4ocs arrangement of prismatic resonators, the smallest gap between resonators is the diagonal, which is 11.3 mm from one corner of the resonator base to the other (see Figure 3-8). This distance is approximately the same as the wavelength of the A_0 Lamb wave mode at 72 kHz, so any wave with a frequency that is higher than this would have a wavelength that is smaller than the smallest gap between resonators in this arrangement. This means more wavelengths of higher frequency waves can fit between the resonators, which potentially explains why the upper bandgap is affected more than the lower bandgap. There are also fewer resonators in this arrangement, so it is expected that the bandgap width would be smaller [5], which can be seen in the lower bandgap.

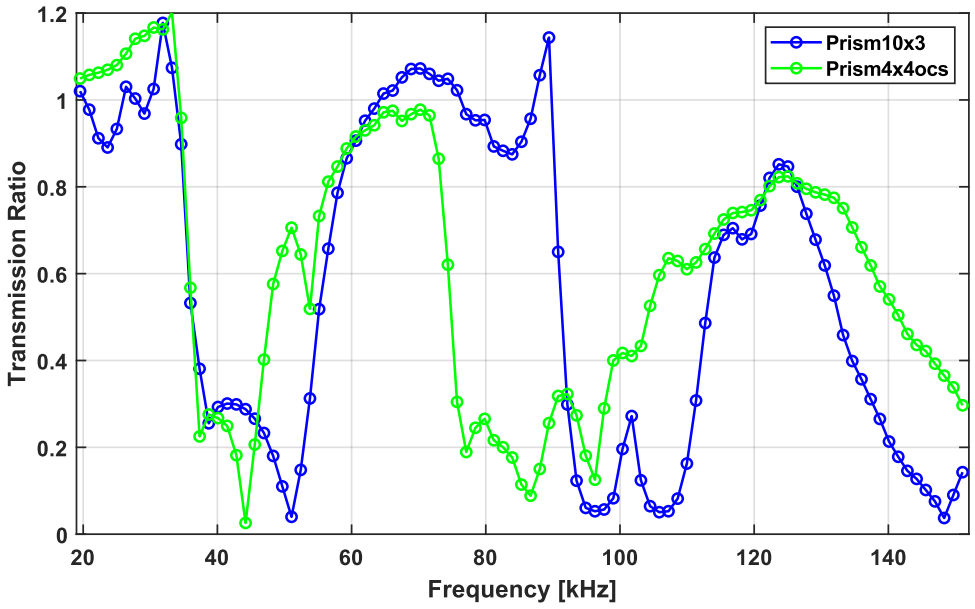

Figure **5-2**: Transmission spectra for numerical results of a metasurface with in-line (10x3) and staggered (4x4ocs) arrangements of prismatic resonators

5.1.2 Connection to Frequency Response Function

The primary motivation for this study is to establish a connection between the frequency response function of the resonator to the transmission spectrum of the corresponding metasurface. As seen in Figure 5-3, the antiresonances at 41.5 kHz and 102 kHz are located within the bandgaps, which validates the idea of the antiresonances inducing clamping boundary conditions that create the bandgaps [4]. The next highest corresponding resonances at 57 kHz and 115.5 kHz seem to line up with the upper limits of each bandgap. From this observation, it is reasonable to assume that the bandgap cannot be larger than the distance between the antiresonance and the next closest resonance. Therefore, it is theorized that by increasing the distance between the antiresonance and the surrounding resonances, the bandgap would likely also increase. Using this relationship, a procedure for topology optimization could be developed to generate resonators for creating a metasurface with an enhanced bandgap.

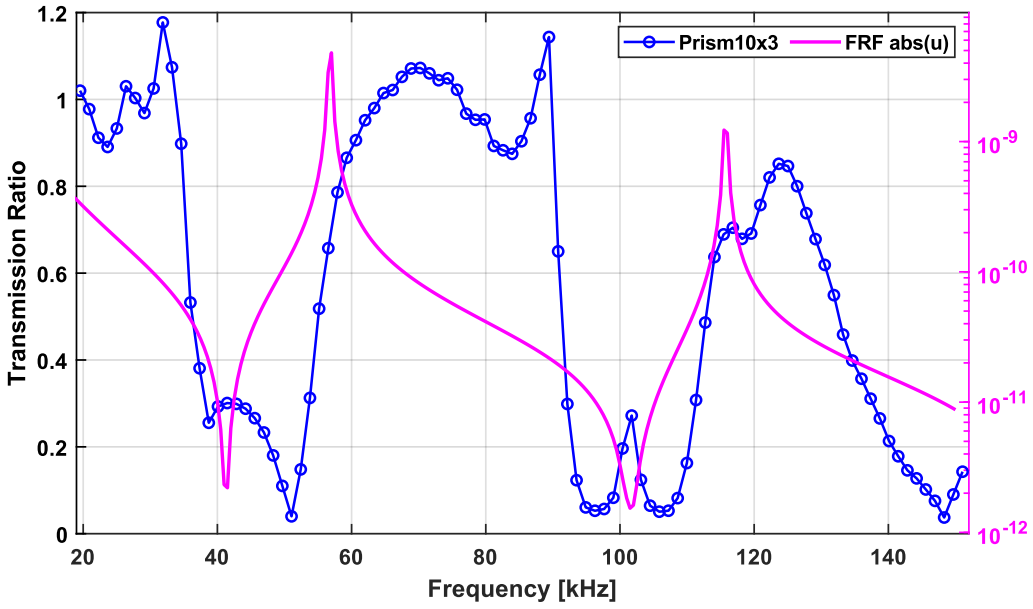

Figure **5-3**: Transmission spectrum for 10x3 arrangement of prismatic resonator with overlayed plot of the frequency response function for the u-component displacement at the resonator base

Chapter 6 Topology Optimization Results and Discussion

Thanks to Daniel Giraldo Guzman for running the topology optimization and providing the following information regarding the objective function and constraints on the process that generated the optimized resonator used in this study [31]. After establishing a connection between the frequency response function and the transmission spectrum, it is reasonable to assume that the FRF could be used to motivate topology optimization with the goal of creating resonators that produce enhanced bandgaps. The resulting topology optimization uses this concept to generate a new resonator design, which was named the Lemon, by pushing the resonances away from the antiresonance in the FRF of the resonator.

6.1 Designing the Optimization

To drive the optimization process, an objective function needs to be established that will accomplish two goals: the location of the bandgap needs to be determined and the resonances in the FRF need to be pushed apart (see Equation 6-1). An appropriate objective function can therefore be written as,

$$min\left[w_1\left(\frac{f_A - f_T}{f_T}\right)^2 + w_2\left|\left(\frac{f_A}{f_R - f_A}\right)\right|\right] \quad \textbf{(6-1)}$$

where w_1 and w_2 are weighting factors, f_T is the desired antiresonance frequency to determine where the bandgap would be located, f_A is the calculated antiresonance frequency, and f_R is the calculated resonance frequency. By trying to minimize the value of this function, the optimization has a parameter to use for determining changes between iterations. In this case, the desired antiresonance frequency is set to 50 kHz, and the optimization is set to calculate the frequency response function between 10 and 150 kHz. The maximum distance between the

resonances cannot be larger than the observed range. The weighting factors w_1 and w_2 are set to 100 and 1 respectively to increase the sensitivity of the first term in the optimization compared to the second term. Figure 6-1 shows how each part of the objective function would look when plotted with their respective weighting factors.

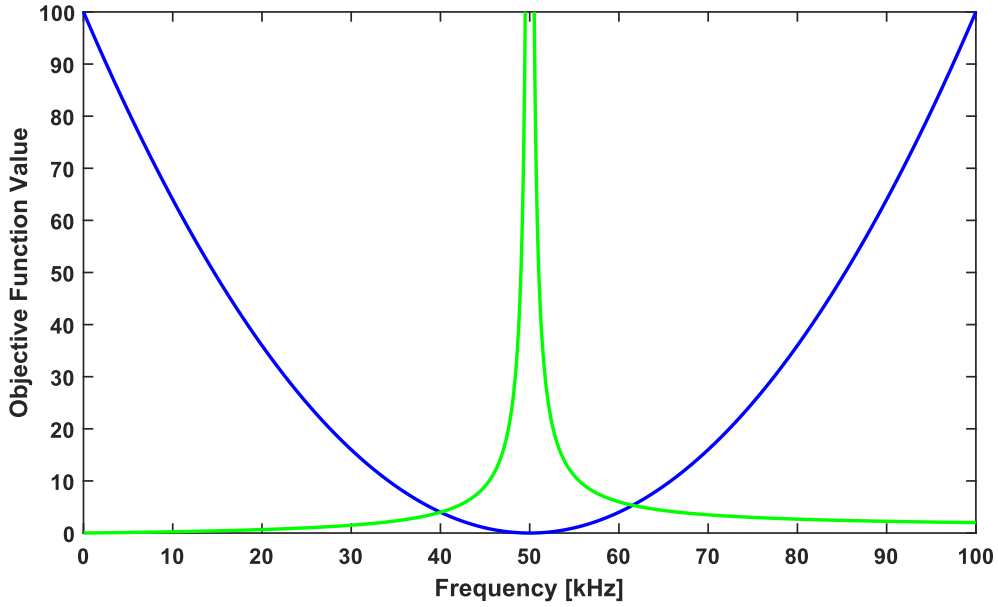

Figure **6-1**: Graphical representation of the objective function used to create the Lemon resonator (see Equation 6-1)

In addition to the objective function, the optimization also considers a variety of restrictions on the geometry of the resonator to prevent overly large or otherwise unrealistic geometries. Table 6-1 outlines these additional restrictions and their set values as well as the material properties that resulted in the Lemon resonator.

Table **6-1**: Geometric restrictions on the optimization process that generated the Lemon resonator

Parameters	Values
Maximum Resonator Size	24 x 24 x 24 [mm]
Base Size	6 x 6 [mm]
Density (ρ)	2730 [kg/m^3]
Elastic Modulus (E)	69 [GPa]
Poisson's Ratio (ν)	0.33

6.2 Lemon Resonator

The optimization resulted in a single mass that, after post-processing to smooth the mesh, looks somewhat like a lemon (see Figure 6-2). After post-processing, the resonator loses some mass, which moves its antiresonance frequency down slightly, so the overall size of the resonator is scaled up by 1.115 to bring the antiresonance back to the desired 50 kHz target. After scaling, the base of this resonator is approximately 7.4 mm x 7.25 mm, which is comparable to the base of the prismatic resonator (see Figure 6-3). However, the overall volume of this resonator is significantly larger than that of the prismatic resonator, and it was not possible to fit the geometry together as closely as in the 10x3 arrangement used for the prismatic resonators. Therefore, an off-centered, staggered arrangement was used to fit these resonators together as closely as possible. This same arrangement can be seen in Figure 3-8, and it was this Lemon resonator that influenced the exact dimensions for that array pattern.

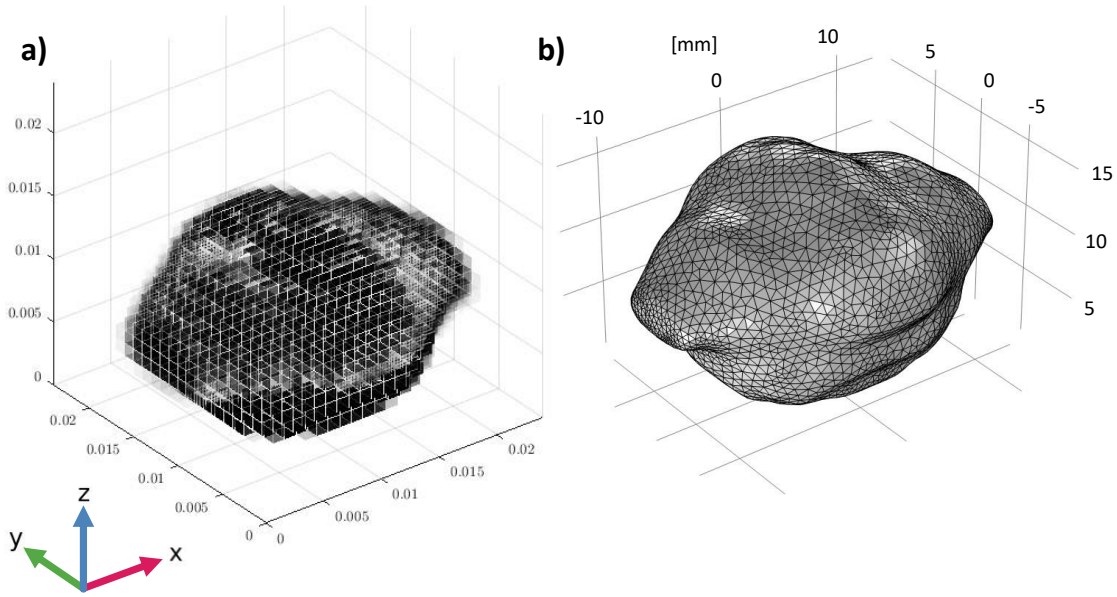

Figure **6-2**: 3D renderings of a) rough topology as determined directly from the optimization and b) the post-processed topology in COMSOL [31]

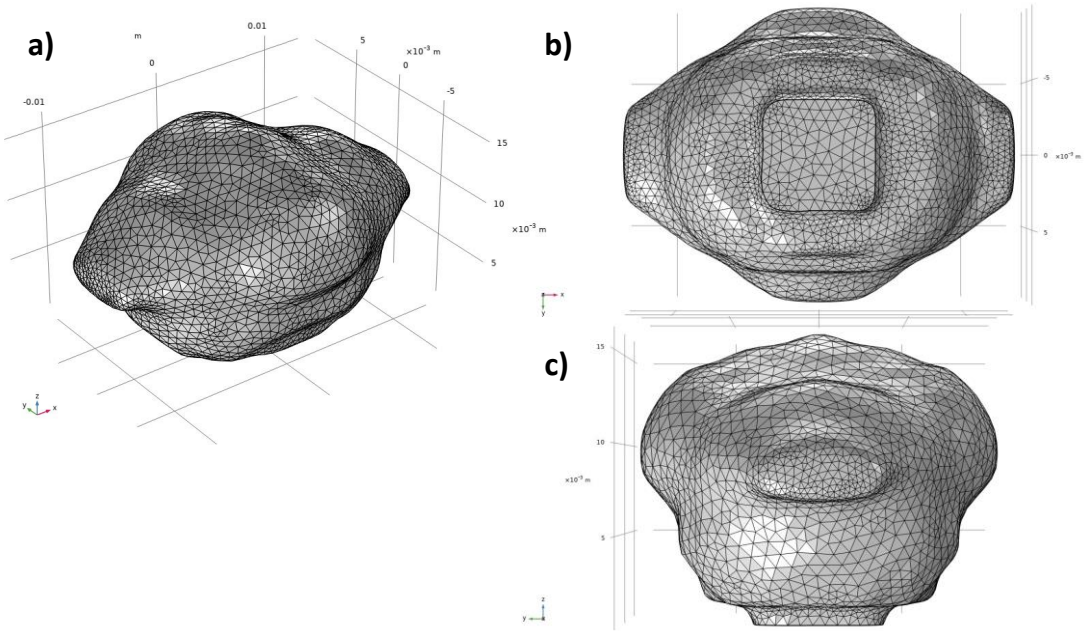

Figure **6-3**: 3D renderings of a) isometric view b) bottom view and c) side view of the Lemon resonator with mesh used in calculating the FRF

6.3 Expanding the Bandgap

As designed in the optimization, the FRF of the Lemon resonator under horizontal, harmonic excitation shows that the resonances have been pushed away from the antiresonance at 50 kHz (see Figure 6-4). Similarly, the dispersion curves for the Lemon resonator on an 11 mm x 11-mm plate show that there should be a wide bandgap for the S_0 mode between 40 and 130 kHz (see Figure 6-5). However, the unit cell used in the dispersion analysis is smaller than the lattice size used in the metasurface arrangement, so the predicted bandgap from the dispersion analysis is not expected to be as accurate as with the prismatic resonators. Nevertheless, the bandgap is predicted to be wider than the prismatic resonators.

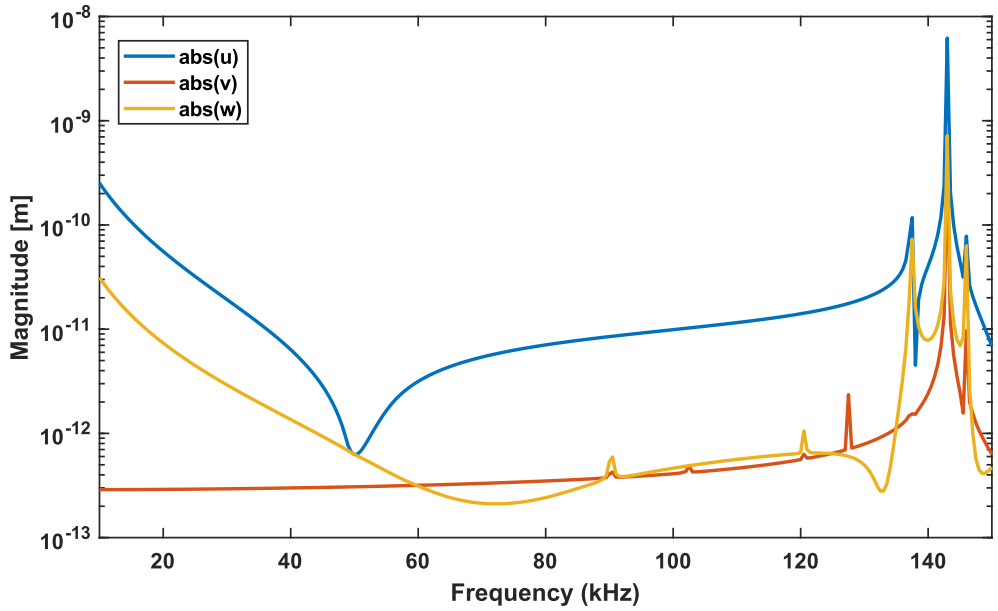

Figure **6-4**: Frequency response function for the Lemon resonator under horizontal, harmonic excitation

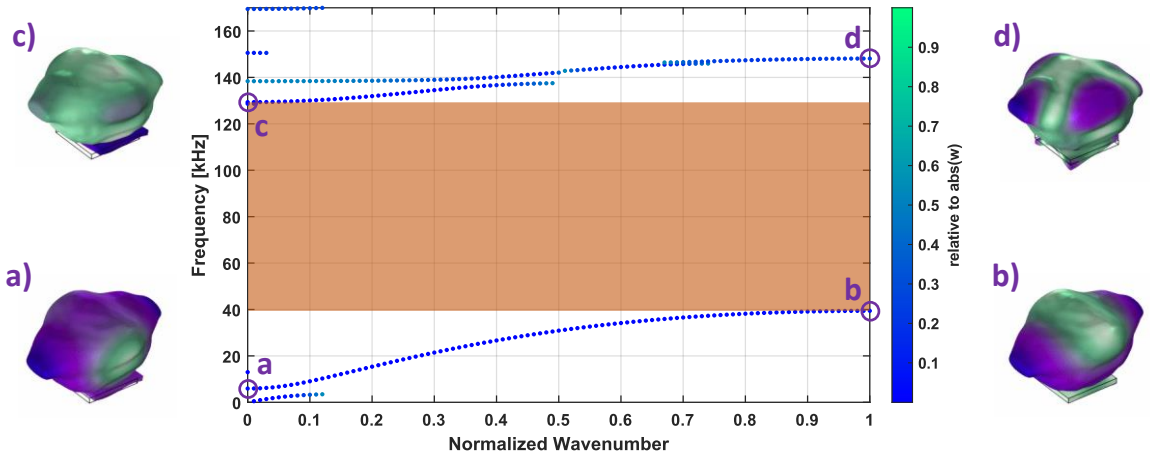

Figure **6-5**: Dispersion curves for the Lemon resonator attached to an 11 mm x 11 mm section of plate showing an enhanced S_0 mode bandgap

6.3.1 Lemon Resonator Bandgap

Using the same numerical analysis as used for the prismatic resonators, the Lemon resonator was shown to have a bandgap between approximately 28 kHz and 70 kHz (see Figure 6-6). However, the dispersion analysis indicated a larger bandgap between 40 kHz and 130 kHz. Similarly, the frequency response function also indicated a larger bandgap that should include 50 kHz and have an upper bound of about 137 kHz (see Figure 6-7). As seen in both Figures 6-6 and 6-7, there appears to be a region between approximately 70 kHz and 110 kHz where the transmission spectrum of the metasurface does not match with the expected bandgaps from either the dispersion analysis or the FRF, but the dispersion analysis and FRF both seem to match well with each other.

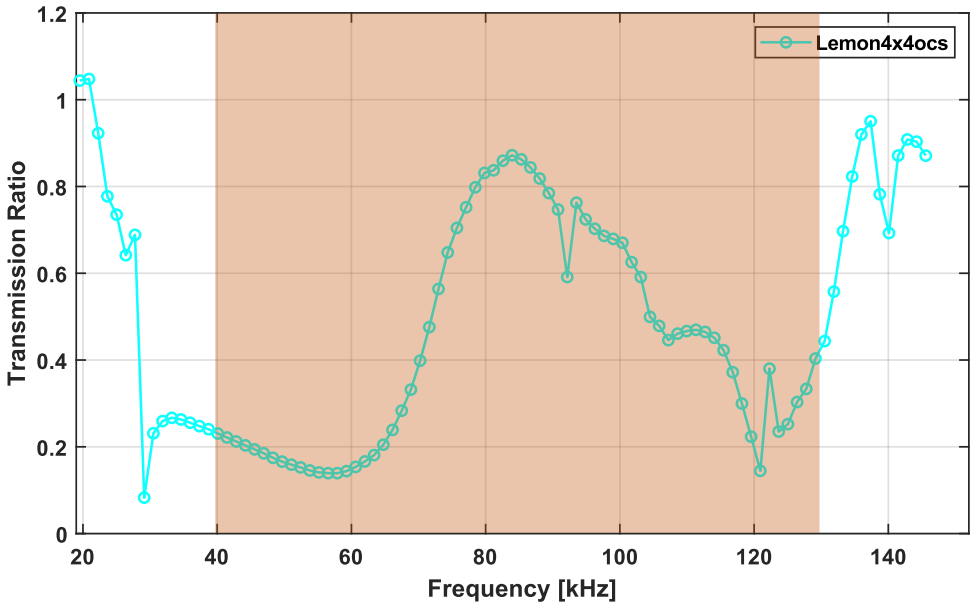

Figure **6-6**: Transmission spectrum for numerical results of a 4x4ocs arrangement of Lemon resonators with highlighted bandgap from dispersion analysis

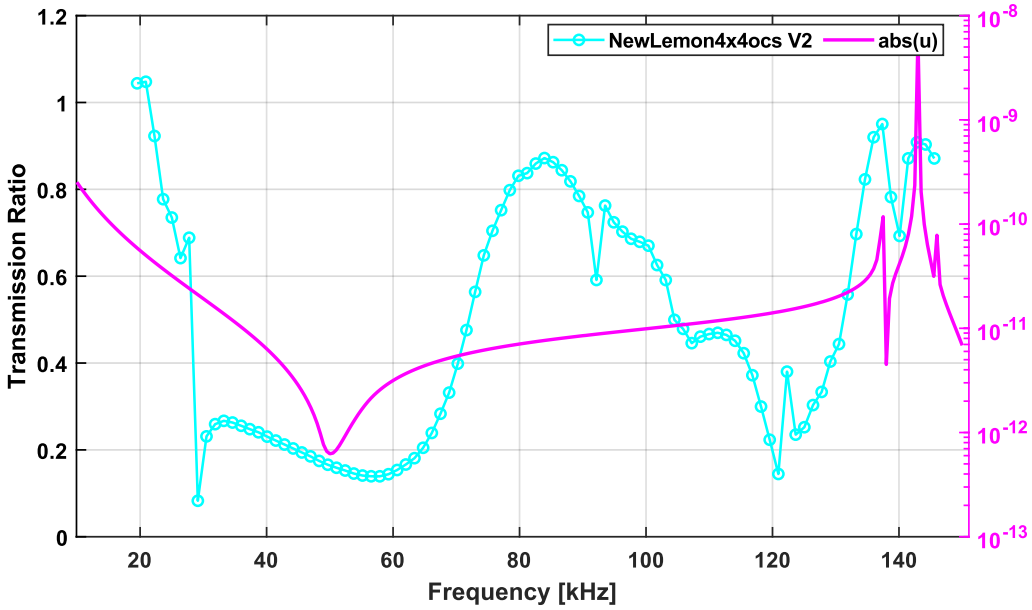

Figure **6-7**: Transmission spectrum for numerical results of a 4x4ocs arrangement of Lemon resonators with frequency response function in the x-direction

The difference between the prediction of the bandgap and the observed bandgap in the transmission spectrum is thought to be a result of the resonator spacing. The arrangement used in the metasurface model packs the resonators as close together as possible, but the dispersion analysis assumes a smaller unit cell size that would match the spacing used in the 10x3 arrangement, which is not physically possible with the larger volume of the Lemon resonators. This larger spacing was not necessary for the prismatic resonators because their volume fit completely above their base area. The Lemon, however, has material that overhangs its base, which limits the total contact area between the resonators and the plate. It is believed that if the resonators could be placed closer together to be more like the 10x3 arrangement that was used for the prismatic resonators, then the bandgaps in the transmission spectrum would match better with the dispersion analysis bandgaps and FRF.

The exact mechanism that causes this anomaly with larger resonator spacing is not fully understood, but it is possibly a result of Bragg Scattering because the spacing between the resonators is approximately the same distance as the wavelength of the A_0 Lamb wave mode at 70 kHz. This effect was not a problem for the prismatic resonators because the spacing between them in the 10x3 arrangement was at most half of a wavelength for the A_0 mode for frequencies below 150 kHz.

6.3.2 Resonator Comparison

Although the metasurface created from Lemon resonators does not have the widest possible bandgap as indicated by the FRF and dispersion curves, the method of pushing the resonances did result in a wider bandgap compared to the prismatic resonator. For this comparison, the edges of the bandgap are determined by the points where the transmission drops below 0.4 (i.e. 40% of the transmission of the S_0 Lamb wave mode in the baseline without

resonators). As seen in Figure 6-8, the targeted bandgap for the Lemon resonator shows a bandwidth of about 41.8 kHz while the prismatic resonator shows a bandwidth of 17.3 kHz for the lower bandgap. Therefore, the Lemon resonator shows a 142% increase in bandwidth compared to the prismatic resonator. The difference is even larger when comparing both Lemon and prismatic resonators in the same arrangement with approximately the same total contact area on the plate and the same total number of resonators. As seen in Figure 6-9, prismatic resonators only show a bandwidth of about 10.3 kHz, which means the Lemon resonators show a 306% increase in the bandwidth by comparison. These results indicate that the topology optimization rationale of pushing the resonances away from the targeted antiresonance still increases the bandgap.

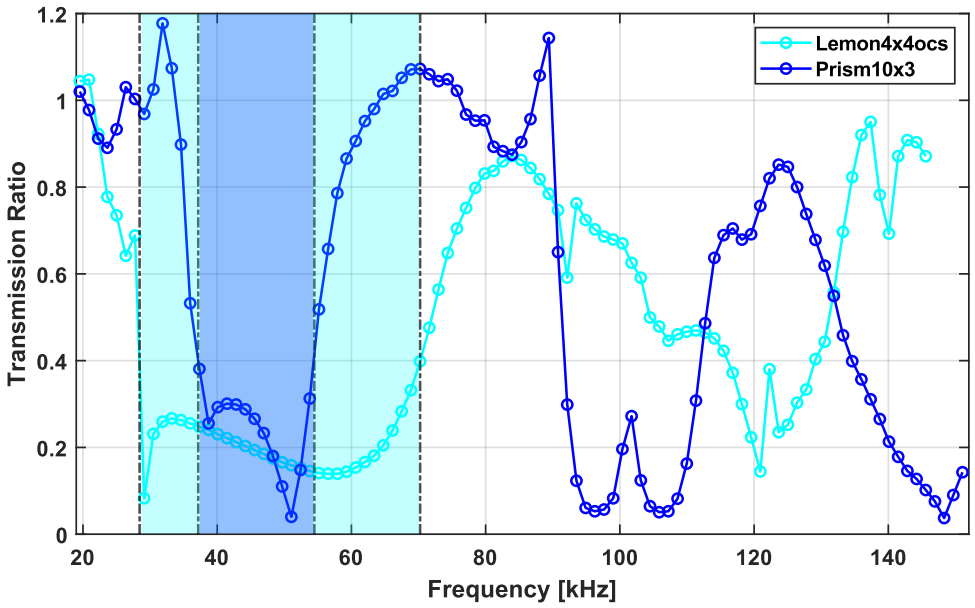

Figure **6-8**: Transmission spectra for numerical results of metasurfaces with 4x4ocs arrangement of Lemon resonators and 10x3 arrangement of prismatic resonators

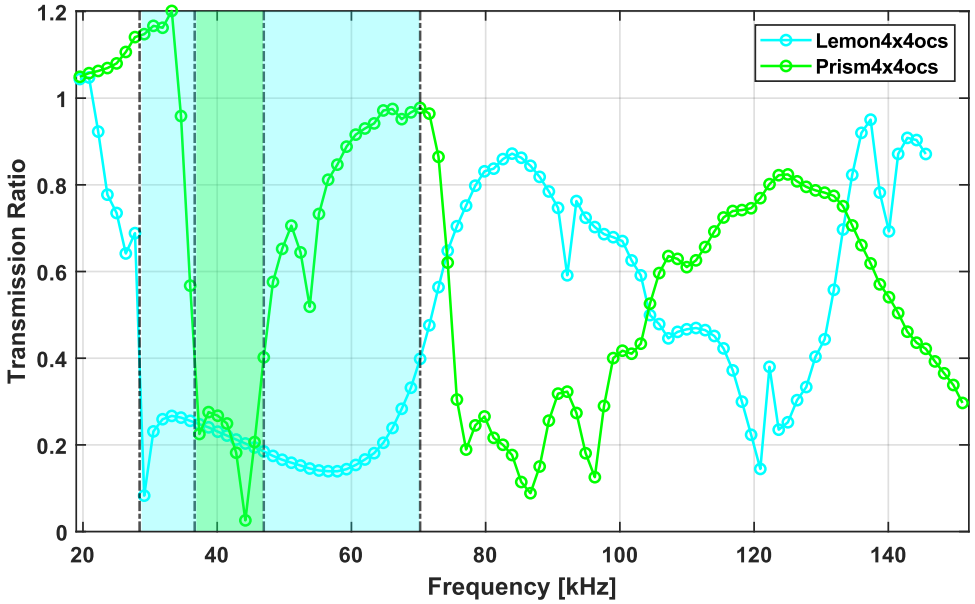

Figure **6-9**: Transmission spectra for numerical results for metasurfaces with 4x4ocs arrangement of Lemon resonators and 4x4ocs arrangement of prismatic resonators

Chapter 7 Conclusion

This study showed that there is a connection between the frequency response function of a single resonator under horizontal, harmonic excitation at the base and the transmission spectrum for the S_0 Lamb wave mode of a metasurface built using an array of the same resonator. Specifically, the antiresonance in the frequency response function determines the location of the stop-bandgap in the transmission spectrum while the resonance determines the boundary of how wide the bandgap can be. Both numerical and experimental methods were used to prove this relationship for a simple metasurface design using prismatic resonators. Using this relationship, a topology-optimized resonator could be designed by aiming to push the resonances away from the targeted antiresonance. The optimized resonator results in a wider bandgap compared to the prismatic resonator, however, additional parameters also seem to influence the bandgap of the final metasurface. One potential factor is the spacing between resonators and, consequently, the arrangement resulting in gaps that are greater than the wavelength of the A_0 mode or both A_0 and S_0 modes that allows for leakage or resonances between the resonators. It is also possible that having different kinds of symmetry in the resonators could also have an influence on the bandgap. Therefore, future work may focus more on the geometric restrictions placed on the topology optimization process to promote the generation of resonators that have a larger base area compared to their volume and may be symmetric about more than one plane.

This study was limited by not looking at the A_0 Lamb wave mode beyond initial tests to ensure the excitation was possible experimentally and numerically. Further investigation may be done to apply similar methods to determine a comparable relationship for the A_0 mode. Similarly, a future study in resonators that may produce bandgaps for both S_0 and A_0 Lamb wave modes may be beneficial for developing more versatile resonator geometries. It can be seen in

the wavenumber spectra that noticeable mode conversion from S_0 to A_0 modes is possible at different frequencies, but this phenomenon was not explicitly studied in this project. Future work may also look more in depth into how the energy from the incident wave is distributed between pure reflection, mode conversion, or energy dissipation because of the metasurface.

Metamaterials, and subsequently metasurfaces, can have beneficial effects and properties in the field of structural mechanics and vibration control. As understanding of the causes of phenomena related to these structures improves, the process by which they are designed will become more standardized and methodical, which will enable more widespread use and open the door for nonintuitive, novel designs for a variety of applications.

Appendix A

MATLAB LiveLink Code

```
% Frequency-dependent wavestructure model creation and export

% General Notes:
% for running in MATLAB LiveLink only
% run each section separately (use "Run Section" or CTRL+ENTER)
% run each section sequentially
% comments on the right side signify places where changes may need to be
% made by the user to change model parameters or folder locations in ROAR
% Collab
% Code created by Jeremy D. Keirn (last edited 06 October 2023)

% Opening MATLAB LiveLink:
% use "Roar Collab RHEL8 Interactive Desktop", open the terminal, use
% command "module load comsol matlab", use command "comsol mphserver
% matlab" (may use with or without "-ckl" at the end to prompt teaching
% license)
% NOTE: first time logging in will prompt a password creation, create a
% password, write it down and save it, this password will likely never be
% needed :)

% Procedure:
% --first run "Creating the frequency..." (check frequency range if desired)
% --second run "Creating the wavestructure..." (comment out "Build Mesh"
% section if desired to save time)
% --go to the cluster, call the chosen directory for running files, use
% command "sbatch COMSOL.sh" to run all models (the models should appear in
% the job list shortly)
% --when models are finished running, go to the running folder and run
% "Exporting..." (this section should run regardless of if all models were
% successful, but it is highly recommended that it is checked that all
% models were completed sucessfully before running (check by looking to
% see if all "zWavestructure_#.mph" files exist and/or if all recovery
% files are 0 bytes in size))

%% Creating the frequency, wavenumber, and stress vectors/matrices
                                                                          %
!!!!!open folder where saving master files and stresses!!!!!
s = 4;                                                                    %
set step for frequency range (must be integer >= 1)
range = 58:s:442;                                                         %
set frequency range (limits: 30 to 450)

% load and sort wavestructure stresses based on range and s               %
DO NOT CHANGE...
```

```
load('Stresses630450.mat');
data = Stresses630450;
smatrix2 = [data(:,1), data(:,(range(1)-30)*12+2:1:(range(end)-29)*12+1)];
ind3 = 0;
ind2 = 0;
smatrix(:,1) = smatrix2(:,1);
for k = range
   smatrix(:,ind3*12+2:1:ind3*12+13) = smatrix2(:,ind2*12+2:1:ind2*12+13);
   ind3=ind3+1;
   ind2=ind3*s;
end

% load and sort frequency and wavenumbers based on range and s
load('freqwav1mmplateS0A0.mat')
data2 = freqwav1mmplateS0A0;
fvector = real(data2((range(1):s:range(end)),1));
kvectorS0 = data2((range(1):s:range(end)),2);
kvectorA0 = data2((range(1):s:range(end)),3);

% save sorted wavestructure matrix for import into COMSOL
save('smatrix.csv','smatrix','-ascii','-double')

% display frequency range parameters for checking
fprintf('Frequency Range: %0.2f to %0.2f [kHz]\n',fvector(1)*1e-
3,fvector(end)*1e-3)
fprintf('Frequency Resolution: %0.2f [kHz]\n',fvector(2)*1e-3-fvector(1)*1e-3)
fprintf('Frequency Resolution: %0.2f [kHz]\n',fvector(end)*1e-3-fvector(end-
1)*1e-3)

%% Creating the wavestructure models

filepath = ['/scratch/jdk5633/Currently_Running/' ...
    'WavestructureV2_Prismatic10x3/'];                                    %
filepath for saving the models for running (will create the folder
automatically)
name = 'Prism10x3_V2';                                                    %
name for batch run (shows up in job list from cluster)
model = mphload('WavestructureV2_Prismatic10x3.mph');                     %
set master file for the model to be run (saved in current open folder)


model.func('int1').set('filename', ...                                    %
note the folder location here
    '/storage/work/jdk5633/Wavestructure/smatrix.csv');                   %
(should be folder where sorted stresses are saved)
model.func('int2').set('filename', ...                                    %
note the folder location here
    '/storage/work/jdk5633/Wavestructure/smatrix.csv');                   %
(should be folder where sorted stresses are saved)

% import sorted wavestructure stress matrix                               %
DO NOT CHANGE...
model.func('int1').importData;
```

```
model.func('int2').importData;

% set model frequency, wavenumbers, and index within sorted stress matrix
ind = 0;
for i = range
    inds = ind*12;
    ind = ind+1;

    model.param.set('WavenumS0', append(num2str(kvectorS0(ind)),' [rad/m]'));
    model.param.set('WavenumA0', append(num2str(kvectorA0(ind)),' [rad/m]'));
    model.param.set('freq_study', append(num2str(fvector(ind)),' [Hz]'));
    model.func('int1').setIndex('funcs', inds+1, 0, 1);
    model.func('int1').setIndex('funcs', inds+2, 1, 1);
    model.func('int1').setIndex('funcs', inds+3, 2, 1);
    model.func('int1').setIndex('funcs', inds+4, 3, 1);
    model.func('int1').setIndex('funcs', inds+5, 4, 1);
    model.func('int1').setIndex('funcs', inds+6, 5, 1);
    model.func('int1').setIndex('funcs', inds+7, 6, 1);
    model.func('int1').setIndex('funcs', inds+8, 7, 1);
    model.func('int1').setIndex('funcs', inds+9, 8, 1);
    model.func('int1').setIndex('funcs', inds+10, 9, 1);
    model.func('int1').setIndex('funcs', inds+11, 10, 1);
    model.func('int1').setIndex('funcs', inds+12, 11, 1);

    % evaluate select parameters for checking
    Wavenum = mphevaluate(model, 'Wavenum');
    freq_study = mphevaluate(model, 'freq_study');
    N_TR = mphevaluate(model, 'N_TR');
    lambda_min = mphevaluate(model, 'lambda_min');
    lambda_max = mphevaluate(model, 'lambda_max');
                                                                        %
Build Mesh and print the mesh statistics (may be commented out to save time)
    model.component('comp1').mesh('mesh1').run;
    stats = mphmeshstats(model,'mesh1');
    Meshstatus(ind) = stats.iscomplete;
    if stats.iscomplete==1
        fprintf('Mesh Complete: %i\n',i)
        numelem_tet = stats.numelem(strcmp(stats.types,'tet'));
        numelem_hex = stats.numelem(strcmp(stats.types,'hex'));
        fprintf('Number of Elements: %i\n',numelem_tet+numelem_hex)
    else
        fprintf('MESH FAILED: %i\n',i)
    end
                                                                        %
End of "Build Mesh" section of code (end commented section here if saving
time)

    % display select parameters for checking
    fprintf('f=%0.4f [kHz] k=%0.2f [rad/m] maxwl=%0.4f [mm] minwl=%0.4f [mm]
N_TR=%i\n\n',...
        freq_study*1e-3,Wavenum,lambda_max*1e3,lambda_min*1e3,N_TR)
    mphsave(model, append(filepath,'Wavestructure_',num2str(i),'.mph'));
end
```

```
% creating .sh scripts
range2 = range;
range_end = 0;

% create overall COMSOL.sh script that runs other scripts
yay = '';
save(append(filepath,'COMSOL.sh'),'yay','-ascii')
fileID2 = fopen(append(filepath,'COMSOL.sh'),'w');

fprintf(fileID2,'#!/bin/bash\n');
fprintf(fileID2,'\n#SBATCH --nodes=1\n');
fprintf(fileID2,'#SBATCH --ntasks-per-node=20\n');
fprintf(fileID2,'#SBATCH --mem=320GB\n');                                    %
note the RAM here (not recommended to go above 640GB or below 160GB) (max
allowed for each user account is about 800GB)
fprintf(fileID2,'#SBATCH --partition=open\n');
fprintf(fileID2,'#SBATCH --output=%%x.out\n');
fprintf(fileID2,'#SBATCH --error=%%x.err\n');
fprintf(fileID2,'\n#SBATCH --time=00:01:00\n');
fprintf(fileID2,'\ncd $SLURM_SUBMIT_DIR\n');

% divide models to be run into four scripts for running
for fileind = 1:1:4
    clear range
    if (fileind*ceil(length(range2)/4)<length(range2))
        range = range2(range_end+1:1:fileind*ceil(length(range2)/4));
        range_end = fileind*ceil(length(range2)/4);
    else
        range = range2(range_end+1:1:end);
    end

    save(append(filepath,'COMSOL_',num2str(range(1)),'_',num2str(s),'_', ...
        num2str(range(end)),'.sh'),'yay','-ascii')
    fileID = fopen(append(filepath,'COMSOL_',num2str(range(1)),'_', ...
        num2str(s),'_',num2str(range(end)),'.sh'),'w');
                                                                             %
change necessary parameters of the .sh script as needed to run in cluster
    fprintf(fileID,'#!/bin/bash\n');
    fprintf(fileID,append('#SBATCH --job-
name=',name,'_',num2str(fileind),'\n'));
    fprintf(fileID,'\n#SBATCH --nodes=1\n');
    fprintf(fileID,'#SBATCH --ntasks-per-node=20\n');
    fprintf(fileID,'#SBATCH --mem=320GB\n');                                 %
note the RAM here (not recommended to go above 640GB or below 160GB) (max
allowed for each user account is about 800GB)
    fprintf(fileID,'#SBATCH --partition=open\n');
    fprintf(fileID,'#SBATCH --output=%%x.out\n');
    fprintf(fileID,'#SBATCH --error=%%x.err\n');
    fprintf(fileID,'\n#SBATCH --time=24:00:00\n');                           %
note the run time here (max allowed time per job is 48:00:00)
    fprintf(fileID,'##SBATCH --begin=13:59\n');
```

```
    fprintf(fileID,'#SBATCH --mail-type=BEGIN,END,FAIL\n');                % 
comment out if email updates are not desired (see next line too)
    fprintf(fileID,'#SBATCH --mail-user=jdk5633@psu.edu\n');               % 
note the email here (change to current user's email) (comment out if email 
updates are not desired)
    fprintf(fileID,'\necho " "\necho "Job started on ''hostname'' at 
''date''"\necho " "\n');
    fprintf(fileID,'\nmodule purge\n');
    fprintf(fileID,'module load comsol\n');
    fprintf(fileID,'\ncd $SLURM_SUBMIT_DIR\n');

    for r = range
        fprintf(fileID,['comsol batch -nn 5 -nnhost 5 -np 4' ...
            ' -mpibootstrap ssh' ...
            ' -inputfile Wavestructure_%i.mph' ...
            ' -outputfile zWavestructure_%i.mph' ...
            ' -tmpdir /scratch/jdk5633/temp%i' ...                         % 
note the folder location here (change to current user preference)
            ' -recoverydir /scratch/jdk5633/temp%i' ...                    % 
note the folder location here (change to current user preference)
            ' -batchlog COMSOL_logfile_%i.log\n'],r,r,fileind,fileind,r);
    end

    fprintf(fileID,'\necho " "\necho "Job Ended at ''date''"\necho " "\n\n');

    fclose(fileID);

    fprintf(fileID2,append('sbatch 
COMSOL_',num2str(range(1)),'_',num2str(s),'_', ...
        num2str(range(end)),'.sh\n'));

end
fclose(fileID2);


%% Exporting the data
                                                                           % 
!!!!!change open folder to where the run models are located!!!!!
step = 4;                                                                  % 
set step for frequency range
range = 58:step:442;                                                       % 
set frequency range
resname = 'Prismatic10x3_V2';                                              % 
set resonator name for export saving (folder must be created manually first 
(will not happen automatically))

filepath = append('/scratch/jdk5633/Currently_Running/',resname,'/');      % 
note the folder location here (change to current user running folder)

                                                                           % 
DO NOT CHANGE...
```

```
surfname =
append(filepath,resname,'_',num2str(range(1)),'_',num2str(step),'_',num2str(ra
nge(end)),'_surfdata.csv');
ind = 0;
for j = range
    testname = append('zWavestructure_',num2str(j),'.mph');
    test = exist(testname, 'file');
    ind = ind+1;
    if test == 2
        clear model
        model = mphload(append('zWavestructure_',num2str(j),'.mph'));

        % setup for saving resonator base response
        %model.result.dataset('surf2').selection.set(128);
        model.result.table.create('tbl1','Table');
        model.result.numerical('av1').set('table', 'tbl1');
        model.result.numerical('av1').setResult
        model.result.export.create('tbl1', 'Table');
        model.result.export('tbl1').set('table', 'tbl1');
        model.result.export('tbl1').set('header', 'off');
        model.result.export('tbl1').set('filename',...

append('/storage/home/jdk5633/scratch/surf_average/surf_average_',num2str(j),'
.txt'));

        % setup for saving incident and transmitted region displacements
        model.result.export('data1').set('filename',...
            append(filepath,'Incident_',num2str(j),'.txt'));
        model.result.export('data2').set('filename',...
            append(filepath,'Transmitted_',num2str(j),'.txt'));

        % export
        model.result.export('tbl1').run
        model.result.export('data1').run
        model.result.export('data2').run

        % append to base response file for final saving in a single file
        fileID =
fopen(append('/storage/home/jdk5633/scratch/surf_average/surf_average_',num2st
r(j),'.txt'));
        tempsurf = fscanf(fileID,'%f');
        surf(:,ind) = tempsurf(:,1);
        fclose(fileID);

        %mphsave(model, append('zzWavestructure_',num2str(j),'.mph'));
        fprintf('%i\n',j)
    else
        fprintf('Model Failed: %i\n',j)
    end
end

% save final base response file
save(surfname,'surf','-ascii','-double')
```

Bibliography

[1] Rupin, Matthieu, Fabrice Lemoult, Geoffroy Lerosey, and Philippe Roux. "Experimental Demonstration of Ordered and Disordered Multiresonant Metamaterials for Lamb Waves." *Physical Review Letters* 112, no. 23 (June 10, 2014): 234301. https://doi.org/10.1103/PhysRevLett.112.234301.

[2] Williams, Earl G., Philippe Roux, Matthieu Rupin, and W. A. Kuperman. "Theory of Multiresonant Metamaterials for A 0 Lamb Waves." *Physical Review B* 91, no. 10 (March 23, 2015): 104307. https://doi.org/10.1103/PhysRevB.91.104307.

[3] Hakoda, Christopher, Cliff J. Lissenden, and Parisa Shokouhi. "Clamping Resonators for Low-Frequency S0 Lamb Wave Reflection." *Applied Sciences* 9, no. 2 (January 2019): 257. https://doi.org/10.3390/app9020257.

[4] Lissenden, Cliff J., Christopher N. Hakoda, and Parisa Shokouhi. "Control of Low-Frequency Lamb Wave Propagation in Plates by Boundary Condition Manipulation." *Journal of Applied Physics* 129, no. 9 (March 4, 2021): 094903. https://doi.org/10.1063/5.0042576.

[5] Keirn, Jeremy, and Parisa Shokouhi. "Widening the Frequency Stop-Bandwidth of Metasurfaces for Controlling Lamb Wave Propagation." Pennsylvania State University, 2022.

[6] Celli, Paolo, Behrooz Yousefzadeh, Chiara Daraio, and Stefano Gonella. "Bandgap Widening by Disorder in Rainbow Metamaterials." *Applied Physics Letters* 114, no. 9 (March 4, 2019): 091903. https://doi.org/10.1063/1.5081916.

[7] Krödel, S., N. Thomé, and C. Daraio. "Wide Band-Gap Seismic Metastructures." *Extreme Mechanics Letters* 4 (September 1, 2015): 111–17. https://doi.org/10.1016/j.eml.2015.05.004.

[8] Pillarisetti, Lalith Sai Srinivas, Cliff J. Lissenden, and Parisa Shokouhi. "Understanding the Role of Resonances and Anti-Resonances in Shaping Surface-Wave Bandgaps for Metasurfaces." *Journal of Applied Physics* 132, no. 16 (October 25, 2022): 164901. https://doi.org/10.1063/5.0093083.

[9] Lemoult, Fabrice, Nadège Kaina, Mathias Fink, and Geoffroy Lerosey. "Wave Propagation Control at the Deep Subwavelength Scale in Metamaterials." *Nature Physics* 9, no. 1 (January 2013): 55–60. https://doi.org/10.1038/nphys2480.

[10] Chipouline, Arkadi, and Franko Küppers. *Optical Metamaterials: Qualitative Models: Introduction to Nano-Optics and Optical Metamaterials*. Vol. 211. Springer Series in Optical Sciences. Cham: Springer International Publishing, 2018. https://doi.org/10.1007/978-3-319-77520-3.

[11] Schurig, D., J. J. Mock, B. J. Justice, S. A. Cummer, J. B. Pendry, A. F. Starr, and D. R. Smith. "Metamaterial Electromagnetic Cloak at Microwave Frequencies." *Science* 314, no. 5801 (November 10, 2006): 977–80. https://doi.org/10.1126/science.1133628.

[12] Cummer, Steven A., Johan Christensen, and Andrea Alù. "Controlling Sound with Acoustic Metamaterials." *Nature Reviews Materials* 1, no. 3 (February 16, 2016): 1–13. https://doi.org/10.1038/natrevmats.2016.1.

[13] Ma, Guancong, and Ping Sheng. "Acoustic Metamaterials: From Local Resonances to Broad Horizons." *Science Advances* 2, no. 2 (February 26, 2016): e1501595. https://doi.org/10.1126/sciadv.1501595.

[14] Deymier, P. A. (Ed.) "Acoustic Metamaterials and Phononic Crystals" Springer (2013).

[15] Su, Guangyuan, Zongliang Du, Peng Jiang, and Yongquan Liu. “High-Efficiency Wavefront Manipulation in Thin Plates Using Elastic Metasurfaces beyond the Generalized Snell’s Law.” *Mechanical Systems and Signal Processing* 179 (November 1, 2022): 109391. https://doi.org/10.1016/j.ymssp.2022.109391.

[16] Kim, Shin Young, Woorim Lee, Joong Seok Lee, and Yoon Young Kim. “Longitudinal Wave Steering Using Beam-Type Elastic Metagratings.” *Mechanical Systems and Signal Processing* 156 (July 1, 2021): 107688. https://doi.org/10.1016/j.ymssp.2021.107688.

[17] Su, Xiaoshi, Zhaocheng Lu, and Andrew N. Norris. “Elastic Metasurfaces for Splitting SV- and P-Waves in Elastic Solids.” *Journal of Applied Physics* 123, no. 9 (December 15, 2017): 091701. https://doi.org/10.1063/1.5007731.

[18] Ma, Fuyin, Zhen Huang, Chongrui Liu, and Jiu Hui Wu. “Acoustic Focusing and Imaging via Phononic Crystal and Acoustic Metamaterials.” *Journal of Applied Physics* 131, no. 1 (January 5, 2022): 011103. https://doi.org/10.1063/5.0074503.

[19] Ding, Wei, Tianning Chen, Chen Chen, Dimitrios Chronopoulos, Badreddine Assouar, Yongzheng Wen, and Jian Zhu. “Description of Bandgaps Opening in Chiral Phononic Crystals by Analogy with Thomson Scattering.” *New Journal of Physics* 25, no. 10 (October 2023): 103001. https://doi.org/10.1088/1367-2630/acfc5e.

[20] Banerjee, Arnab, Raj Das, and Emilio P. Calius. “Frequency Graded 1D Metamaterials: A Study on the Attenuation Bands.” *Journal of Applied Physics* 122, no. 7 (August 21, 2017): 075101. https://doi.org/10.1063/1.4998446.

[21] Bilal, Osama R., and Mahmoud I. Hussein. “Trampoline Metamaterial: Local Resonance Enhancement by Springboards.” *Applied Physics Letters* 103, no. 11 (September 9, 2013): 111901. https://doi.org/10.1063/1.4820796.

[22] Sainidou, R., N. Stefanou, and A. Modinos. “Widening of Phononic Transmission Gaps via Anderson Localization.” *Physical Review Letters* 94, no. 20 (May 27, 2005): 205503. https://doi.org/10.1103/PhysRevLett.94.205503.

[23] Coffy, Etienne, Thomas Lavergne, Mahmoud Addouche, Sébastien Euphrasie, Pascal Vairac, and Abdelkrim Khelif. “Ultra-Wide Acoustic Band Gaps in Pillar-Based Phononic Crystal Strips.” *Journal of Applied Physics* 118, no. 21 (December 7, 2015): 214902. https://doi.org/10.1063/1.4936836.

[24] Ponti, Jacopo M. De, Andrea Colombi, Raffaele Ardito, Francesco Braghin, Alberto Corigliano, and Richard V. Craster. “Graded Elastic Metasurface for Enhanced Energy Harvesting.” *New Journal of Physics* 22, no. 1 (January 2020): 013013. https://doi.org/10.1088/1367-2630/ab6062.

[25] Sigmund, Ole, and Kurt Maute. “Topology Optimization Approaches.” *Structural and Multidisciplinary Optimization* 48, no. 6 (December 1, 2013): 1031–55. https://doi.org/10.1007/s00158-013-0978-6.

[26] Giraldo Guzman, Daniel, Lalith Sai Srinivas Pillarisetti, Sashank Sridhar, Cliff J. Lissenden, Mary Frecker, and Parisa Shokouhi. “Design of Resonant Elastodynamic Metasurfaces to Control S0 Lamb Waves Using Topology Optimization.” *JASA Express Letters* 2, no. 11 (November 9, 2022): 115601. https://doi.org/10.1121/10.0015123.

[27] Jung, Jaesoon, Seongyeol Goo, and Junghwan Kook. “Design of a Local Resonator Using Topology Optimization to Tailor Bandgaps in Plate Structures.” *Materials & Design* 191 (June 1, 2020): 108627. https://doi.org/10.1016/j.matdes.2020.108627.

[28] Halkjær, Søren, Ole Sigmund, and Jakob S. Jensen. “Maximizing Band Gaps in Plate Structures.” *Structural and Multidisciplinary Optimization* 32, no. 4 (October 1, 2006): 263–75. https://doi.org/10.1007/s00158-006-0037-7.

[29] Rong, Junjie, and Wenjing Ye. “Multifunctional Elastic Metasurface Design with Topology Optimization.” *Acta Materialia* 185 (February 15, 2020): 382–99. https://doi.org/10.1016/j.actamat.2019.12.017.

[30] Vasseur, Jérôme O. “Periodic Structures, Irreducible Brillouin Zone, Dispersion Relations and the Plane Wave Expansion Method.” In *Acoustic Waves in Periodic Structures, Metamaterials, and Porous Media: From Fundamentals to Industrial Applications*, edited by Noé Jiménez, Olga Umnova, and Jean-Philippe Groby, 3–42. Topics in Applied Physics. Cham: Springer International Publishing, 2021. https://doi.org/10.1007/978-3-030-84300-7_1.

[31] Giraldo Guzman, Daniel, Clifford Lissenden, Parisa Shokouhi, and Mary Frecker. “Topology Optimization Design of Resonant Structures Based on Antiresonance Eigenfrequency Matching Informed by Harmonic Analysis.” *Journal of Mechanical Design* 145, no. 101704 (July 19, 2023). https://doi.org/10.1115/1.4062882.